Particle transport in neutral xenon: 2D modelling approach for the contribution of recombination processes to VUV emissions

J Capeillère, Neermalsing Sewraj, P Ségur, M-C Bordage, Frédéric Marchal

Particle transport in neutral xenon: 2-D modeling approach for the contribution of recombination processes to VUV emissions.

J. Capeillère, N. Sewraj, P. Ségur, M-C. Bordage and F. Marchal

LAboratoire PLAsma et Conversion d'Energie, UMR 5213 CNRS, UPS, INPT,
Université de Toulouse – Paul Sabatier (Toulouse III)
118, route de Narbonne, F-31062 Toulouse cedex 9, France

E-mail: neermalsing.sewraj@laplace.univ-tlse.fr and julien.capeillere@laplace.univ-tlse.fr

Keywords: xenon, ionisation, particle dynamics, excimer, VUV radiation

Submitted to J. Phys. B: At. Mol. Opt. Phys.

Abstract

This paper constitutes a first step in studying transport phenomena, consecutive to a very brief 2-photon excitation of the Xe($^3P_2$) metastable state in neutral xenon, followed by absorption of a further photon leading to ionisation, in Two-Photon Absorption Laser-Induced Fluorescence (TALIF) experiments. Here, the laser beam simply defines the column volume in which electrons and atomic ions are initially confined. Performing a numerical approach, we only consider the reactions occurring once electrons and atomic ions are produced by the incident laser pulse. All metastable atoms initially present are discarded, thus allowing evaluation of the contribution of only recombination processes to the VUV emissions. Besides kinetics of collisional and radiative processes, we also account for diffusion and possible drift phenomena (in presence of a Laplacian electric field). We provide spatial distributions of the number densities of the various species as well as temporal profiles of both their total number and the different VUV emissions. The influence of the external electric field and xenon pressure is discussed as well.

I. Introduction

Intense VUV (Vacuum ultraviolet) and UV (ultraviolet) rare-gas based sources have been developed since the 1980s **[Eli]-[Esr]-[Ber-1]-[Xu]**. Very efficient **[Vol]-[Mil-1]-[Hit]-[Mer-2]** and promising **[Kog-1]**, xenon based sources, emitting around 172 nm, are increasingly used **[Ech]-[Kog-2]** in various fields such as medical care **[Sos]**, environmental protection **[Sos]-[Lun]** material deposition **[Esr]-[Ber-1]-[Buc]** and processing **[Zha]** as well as in mercury-free excimer lamps **[Tra]**.

During the last decades, the kinetics of excited species in neutral rare gases, and more particularly in xenon has been investigated in our laboratory, using the LIF, TALIF and ThALIF (respectively, One-, Two- and Three-Photon Absorption Laser-Induced Fluorescence) techniques **[Sal]-[Ber-2]-[Sew-1]-[Mar-1]-[Led]**. A brief and selective initial excitation is absolutely essential for a reliable kinetic analysis of the spatiotemporal relaxation of the energy of the excited species. Indeed, a spectrally sharp (0.002 nm) and short-pulsed (7 ns) laser beam enables to selectively populate a given state, in particular, the first metastable $Xe(^3P_2)$, by 2-photon excitation of the ground state $Xe(^1S_0)$ atoms **[Led]**. Under such conditions, the initial state of the medium is well determined. All these works led to more or less accurate experimental determinations of certain molecular radiative lifetimes, 3- and 2-body collision rate constants, natural atomic lifetimes of $Kr(^3P_1)$ and $Xe(^3P_1)$ states, Van der Waals broadening coefficients and kinetic schemes.

In these experiments, high intensity laser beams are required **[Sal]-[Ber]-[Sew-1]-[Mar-1]-[Led]**. The absorption of an additional photon can nevertheless ionize the atom provided that the initial excited state is not destroyed. Once created, the atomic ions may undergo 3-body collisions to form molecular ions. With regard to the variety of excited states created through recombination processes, the initial excitation can no more be considered to be selective.

In order to appreciate the influence of the initial ionisation on the kinetics of the medium in LIF, TALIF and ThALIF experiments, we are starting a numerical study of transport phenomena of excited and charged species, including diffusion and drift processes. Our long-term objective is to apprehend the influence of electronic recombination processes on the observed VUV emissions, and consequently on the determination of the relevant lifetimes and collision rate constants, when both excitation and ionisation initially occur.

When suitable excitation conditions are met, the gas is barely ionised and excitation can be considered as being perfectly selective. Under these conditions, the kinetics leading to VUV emissions of xenon has been well established by our team **[Led]**. However, in some particular circumstances, the incident laser photons can completely ionise all the $Xe(^3P_2)$ relay states, and

lead to equal number densities of electrons and mono-atomic xenon ions. The corresponding kinetics resulting to VUV photons stemming only from recombination processes, in such circumstances, has never been reported. According to our first measurements **[Rod]**, the observed kinetics is quite different from those extensively reported when selective excitation is correctly achieved **[Sal]-[Sew-1]-[Led]**.

The present paper constitutes a first study and deals with the phenomena consecutive to only electronic recombination processes. We use a kinetic scheme, in which electronic recombination is simplified via only two reactions. The 2D-numerical code developed for this study is similar to that used to describe a mono-filamentary dielectric barrier discharge (DBD) in nitrogen **[Pot]-[Ces]**, but it was adapted so as to account for the experimental conditions. The main differences concern geometry, physical parameters (pressure, gas temperature,…), gas nature as well as swarm parameters (transport coefficients, mean energies, reaction rates, ...) related to the transport of the species in xenon.

In this paper, our aim is, on the one hand, to understand the evolution of spatiotemporal distributions of all charged and excited species initiated only by recombination processes, and on the other hand, to consequently evaluate the contribution of the various excited species yielding VUV emissions. Here, multi-photonic ionisation should only be regarded as a means to create the initial number densities of the charged particles. Due to a lack of some reliable data concerning two-photon excitation cross-section of the $Xe(^3P_2)$ state and the ionisation cross-section by absorption of a further incident photon, we are unable to provide a realistic initial number density of the charged particles. An experimental determination of these cross-sections is actually under investigation by our team.

Using an arbitrary number density of initial electrons independent of xenon pressure, this 2D modelling provides the contribution of each charged and excited species dynamics through their spatiotemporal number density distributions, which are not accessible at all by experiments. These quantities will allow us to determine the overall temporal evolutions of each emission. The numerical schemes used for this work have already been probated in a previous study **[Pan]**.

In a following paper, this work will be used, in a second step, so as to understand our experimental records where ionisation is complete. It will also enable us to better understand our LIF experiments carried out in xenon, when incomplete ionization nevertheless breaks selectivity, provided the relevant excitation and ionisation cross-sections are well determined.

Finally, in a further third phase we expect that both studies will bring out qualitative trends concerning VUV sources of DBD. We then intend to account for a realistic initial excitation of the main excited species of the discharge in order to make a direct comparison between modelling and experiments For this purpose, we need to improve the time-resolution and

the spectral domain of our DBD setup, with which we have been performing, since 2000, in-situ spectroscopic studies in rare gases based mono-filamentary dielectric barrier discharges (DBDs) **[Mer-1]-[Mer-2]-[Sew-2]-[Mer-3]**. In these VUV plasma sources, electrons are responsible for the initial excitation and ionisation of the gas and greatly influence the discharge properties. Post-discharge kinetics of the filamentary xenon DBD is well established, whereas at initial times many questions still remain unanswered. Whenever required, some basic data will be determined by using LIF, TALIF and ThALIF experiments, which is a powerful tool for accurate measurements of reaction rates.

II. Experimental situation and model formulation

II.1 Experimental situation

The experimental setup, used for our LIF, TALIF and ThALIF experiments where Xe($^3P_2$) atoms are selectively excited, is thoroughly described **[Led]**. A Sirah Cobra Stretch dye-laser (Rhodamine 6G) pumped by the 532 nm harmonic of a Spectra Physics neodymium YAG laser, delivers 7-ns duration photon pulses at a repetition rate of 30 Hz, with a spectral width of 0.002 nm, obtained by using a double grating.

The laser beam (Figure 1.a) crossing the medium between two transverse metallic cylindrical electrodes (radius, *R = 35 mm*) separated by *D = 5 mm*, is here regarded as an axial cylinder whose cross-sectional diameter is *d = 2mm*. For our lowest pressure (*30 Torr*) where diffusion is the maximum, the species remain restricted around the laser beam axis. For each z-position, we consider a rectangular domain: *D = 5 mm* and *L = 15 mm*, along respectively *x* and *y* axes (Figure 1.b). Only within the laser beam-waist (d = 2 mm) which constitutes the laser envelope, Xe($^3P_2$) states are populated by the incident Gaussian (radial) laser beam via absorption of two photons by ground state Xe($^1S_0$) atoms (Figure 2). The long-life Xe($^3P_2$) excited xenon atoms thus created can either produce $Xe_2[1_u(^3P_2)]$ excimers, at their high vibrational levels through 3-body collisions with two Xe($^1S_0$) atoms or absorb a further laser photon to produce $Xe^+(^2P_{3/2})$ atomic ions, according to:

$$Xe(^3P_2) + h\nu_{laser} \longrightarrow Xe^+(^2P_{3/2}) + e^- \qquad (1)$$

The relevant multi-photon excitation and photo-ionisation via the Xe($^3P_2$) relay state are well explained in **[Led]**, where the selection rules, are given as well. We remind that the probability that one Xe($^3P_2$) atom to be ionised is given by $\frac{\sigma_i F}{\sigma_i F + k[Xe(^1S_0)]^2}$, where σ_i is the

cross-section of ionisation (in cm^2) by absorption of a further photon by $Xe(^3P_2)$, F (in $cm^{-2}.s^{-1}$) is the incident laser photon flux, $[Xe(^1S_0)]$ is the number density of $Xe(^1S_0)$, atoms, k is the 3-body formation collisional rate constant of $Xe_2[1_u(^3P_2)]$ excimers, $k\cdot[Xe(^1S_0)]^2$ is their production rate (in s^{-1}) and $\sigma^{(2)}\cdot F$ is the ionisation rate of $Xe(^3P_2)$ atoms. The electron number density is equal to $\sigma^{(2)}F^2[Xe(^1S_0)]\frac{\sigma_i F}{\sigma_i F + k[Xe(^1S_0)]^2}\Delta t$, where $\sigma^{(2)}$ is the excitation cross-section for 2-photon excitation of $Xe(^1S_0)$ atoms (in $cm^4\cdot s$) and Δt is the laser pulse width (7 ns). The photon flux F related to the laser intensity I (in $W\cdot cm^{-2}$): $F = \frac{I}{h\nu}$, and I has a radial Gaussian shape.

When an external field is applied between the metallic electrodes, electrons resulting from (2+1) photo-ionisation can be collected.

If a converging lens is used to focus the laser beam so that $\sigma_i\cdot F >> k\cdot[Xe(^1S_0)]^2$, like in **[Rod]**, then every $Xe(^3P_2)$ atom can be assumed to undergo photo-ionisation, thus leading to a $Xe^+(^2P_{3/2})$ ion . The results reported by **[Rod]** clearly show that the kinetics which then account for VUV photons is very different to those usually encountered when excitation is selectively performed. Due to the converging lens, the beam-waist of the focused laser beam is much narrower and the number of initial electrons may be quite low. A rough estimation of $\sigma^{(2)}$ was attempted by our team **[Led]** but its uncertainty is rather bad. Our value of $\sigma^{(2)}$ is thus not reliable. Besides, σ_i is not well determined, neither. Actually, an experimental determination of both values is under investigation by our team. Provided that these quantities are determined with a good level of confidence, we will be able to calculate the initial electron number density. In this paper, we use an arbitrary value for the maximum of the initial electron density.

The electron number density is given by equation (2).

$$n^*_{0e}(x,y)\big|_{t=0} = n^*_{0\,Xe^+}(x,y)\big|_{t=0} = \begin{cases} n_0 \exp\left[-\frac{(x-x_0)^2}{2\sigma_x^2} - \frac{(y-y_0)^2}{2\sigma_y^2}\right] \text{ if } (x-x_0)^2 + (y-y_0)^2 \le \frac{d^2}{4} \\ 0 \text{ otherwise} \end{cases} \quad (2)$$

where, this distribution, having an amplitude of $n_0 = 10^7$ cm^{-3}, is located at the centre $C(x_0 = 2.5\text{ mm}, y_0 = 7.5\text{ mm})$ of the simulation domain. Its width $\sigma_x = \sigma_y = \sigma = \frac{1\text{ mm}}{2\sqrt{2\ln 2}} \approx 0.42\text{ mm}$ is chosen so as to match the laser beam-waist of 1 mm. To avoid any discontinuity of the electron number density at the laser envelope while assuming that no ionisation occurs outside this domain, equation (2) needs to be modified:

$$n_{0e}(x,y)\big|_{t=0} = n_{0\,Xe^+}(x,y)\big|_{t=0} = n_0 \frac{n^*_{0e}(x,y)\big|_{t=0} - n_{0e,ref}}{n_0 - n_{0e,ref}} \quad (3)$$

where $n_{0e,ref} = n_{0\,Xe^+,ref} = n^*_{0e}(x_0 + \frac{d}{2}, y_0)\Big|_{t=0} = n_0 \exp\left(-\frac{d^2}{8\sigma^2}\right) = 6,25.10^5 \text{ cm}^{-3}$

We note that the transition from relation (2) to (3) causes a slight decrease (4 %) of the laser's beam-waist, without any significant influence on our results. Figure 3 represents the 3D and 2D initial distributions used for the electronic and the atomic ions number density in the $x = x_0$ and $y = y_0$ planes. The above distribution just defines the "column" in which electrons (all having a well defined energy of 0.345 eV), and atomic ions are initially confined, at the initial time t = 0 s. Neither molecular ions nor excited (atomic and molecular) species are supposed to pre-exist in the medium. During experiments, only the temporal evolution of the emitted photon flux can be recorded, whereas our modeling provides additional useful information such as the spatio-temporal distribution of each excited and charged species.

Under suitable experimental conditions, for 2-photon selective excitation of atomic Xe($^3P_2$), ionisation should be avoided. So, preliminary to a kinetic study, an electrical field is applied perpendicularly to the laser beam in order to collect any electron produced by undesired (2+1) photo-ionisation. Therefore, we also studied the influence of an external electric field on the collection of photons. Only a geometric field ($E = 40$ V.cm^{-1}), initially applied along the x direction was taken into account. Indeed, as we considered an initial low particle density (the maximum of the electronic distribution density is equal to 10^7 cm^{-3}), the Debye radius always remains much greater than the characteristic lengths of the domain **[Rai]**. Hence, here the ambipolar diffusion electric field is negligible.

II.2 Kinetic scheme

In order to deal with particle transport while still keeping reasonable calculation times, we adopt the 17-reaction kinetic scheme given in table 1 which includes the main excimers (Figure 4). The starting point is the same initial distribution of $Xe^+(^2P_{3/2})$ atomic ions and electrons particle density, whereas the Xe($^3P_2$) metastable number density is assumed to be null. We remind that the initial mono-energetic electrons (0.345 eV) cannot produce any further excitation of ground state xenon atoms, whose particle number density (N) is calculated from the perfect gas law.

Once (2+1)-photon ionisation occurs, $Xe^+(^2P_{3/2})$ atomic ions can first give rise to molecular ions $Xe_2^+(A^2\Sigma_u^+)$ by three-body collisions with $Xe(^1S_0)$ (reaction R.01 of Table 1). Electronic recombination processes (reactions R.02 and R.03) can then intervene to produce a lot of possible atomic excited states. Similarly to various authors **[Oda]-[Shi]**, we consider only one fictitious excited state Xe(6p), here called 6p (9.73 eV), which is representative of all the upper levels of the many visible transitions issuing from the 6p, 5d, 7s and 6p' states and higher levels towards the 6s and 6s' level **[Moo]**.

For simplification sake, reaction R.08 is dealt with the apparent lifetime (measured with our experimental setup) and thereby we account for the radiation trapping phenomena **[Hol-1]-[Hol-2]-[Pay-1]-[Pay-2]-[Mol]** which depends on experimental conditions **[Sew-1]**.

The reaction rate of electronic recombination of molecular ions (R.03) depends on the mean electron energy. It was obtained by solving Boltzmann's equation as a function of the reduced electric field E/N **[Mat]** (Figure 5). Figure 6 schematizes the kinetic scheme described by table 1.

II.3 Particle transport

The diffusion ($\delta = 0$) and drift-diffusion ($\delta = 1$) equations which describe the spatio-temporal variations of the density $n_q(\vec{r},t)$ at position $\vec{r}$ and time t of every type of particles q (electrons, positive ions and neutral excited species), with or without electric field, respectively, are given by:

$$\frac{\partial n_q}{\partial t}(\vec{r},t) - \vec{\nabla}.\left[\overline{\overline{D}}_q(\vec{r},t).\vec{\nabla} n_q(\vec{r},t)\right] + \delta.\vec{\nabla}.\left[\vec{w}_q(\vec{r},t).n_q(\vec{r},t)\right] = S_q(\vec{r},t) \qquad (4)$$

where $\overline{\overline{D}}_q$ is the diffusion tensor of every type of species q and S_q is the global source term which accounts for the production and the loss of particles intervening in different collisional processes. In the presence of an external electric field $\vec{E}$, $\vec{w}_q = \mu_q \vec{E}$ is the drift velocity of particle q, proportional to its mobility μ_q. In the adopted 2D cartesian geometry, the diagonal diffusion tensor $\overline{\overline{D}}_q$, composed of the transversal diffusion coefficient D_{T_q} (perpendicularly to the electric field) and of the longitudinal one D_{L_q} (in the same direction the electric field), is given by:

$$\overline{\overline{D}}_q = \begin{bmatrix} D_{L_q} & 0 \\ 0 & D_{T_q} \end{bmatrix} \tag{5}$$

We use the local electric field approximation which consists of considering charged particles to be equilibrium with the electric field. Swarm parameters such as mobility (or drift velocity) and diffusion coefficients of species indirectly depend on position and time, via the reduced electric field E/N. In our configurations, with or without a Laplacian field along the $[Ox)$ axis, the transport equations take the following form:

$$\frac{\partial n_q}{\partial t}(x,y,t) - D_{L_q}\left(\frac{E}{N}\right)\frac{\partial^2 n_q}{\partial x^2}(x,y,t) - D_{T_q}\left(\frac{E}{N}\right)\frac{\partial^2 n_q}{\partial y^2}(x,y,t) + \delta.\frac{\partial}{\partial x}\left[w_q\left(\frac{E}{N}\right).n_q(x,y,t)\right] = S_q(x,y,t) \tag{6}$$

The boundary conditions are Neumann's type, given by:

$$\begin{cases} \dfrac{\partial n_q}{\partial x}(0,y,t) = \dfrac{\partial n_q}{\partial x}(D,y,t) = 0 \\ \dfrac{\partial n_q}{\partial y}(x,0,t) = \dfrac{\partial n_q}{\partial y}(x,L,t) = 0 \end{cases} \tag{7}$$

The numerical methods employed to solve the transport equations are given in section II.5. For each species, the total number of particles per unit length along the *z* direction, is calculated by integrating the corresponding number density over the whole simulation domain:

$$N_q(t) = \int_0^D dx \int_0^L dy\, n_q(x,y,t) \tag{8}$$

The VUV emissions are produced by different groups of photons according to their energy range. Each radiation is characterized by a typical central wavelength: resonant photons ($\lambda_{\text{res}} = 147$ nm) coming from the $^3P_1$ radiative de-excitation towards the ground state (Table 1, R.08), photons constituting the first continuum ($\lambda_{1c} = 152$ nm) (Table 1, R.11 and R.13) and the second continuum ($\lambda_{2c} = 172$ nm) (Table 1, R.16 and R.17) of xenon. For calculations, we introduce their quantum energies $h\nu_k$, where k stands for either photons (*res*) or those coming from the first (*1c*) or the second continuum (*2c*). These energies are respectively equal to $1.3523\text{x}10^{-18}$ J (≈ 8.45 eV), $1.3078\text{x}10^{-18}$ J (≈ 8.17 eV) and $1.1557\text{x}10^{-18}$ J (≈ 7.22 eV). The VUV power emitted per unit length is here calculated by:

$$I_{VUV}(t) = h\nu_{\text{res}}\frac{N_{\text{Xe}(^3\text{P}_1)}(t)}{\tau_{\text{Xe}(^3\text{P}_1)}} + h\nu_{1c}\sum_{l=1u_h,0u_h^+}\frac{N_l(t)}{\tau_l} + h\nu_{2c}\sum_{m=1u_b,0u_b^+}\frac{N_m(t)}{\tau_m} \tag{9}$$

where $\tau_{Xe(^3P_1)}$, $\tau_{Xe_2[1_u(^3P_2)]_h}$, $\tau_{Xe_2[1_u(^3P_2)]_b}$, $\tau_{Xe_2[0_u^+(^3P_1)]_h}$ et $\tau_{Xe_2[0_u^+(^3P_1)]_b}$ are the radiative lifetimes of the excited states, responsible for the VUV emissions. In a first approximation, we do not account for the spectral profile of the emission issuing from the $^3P_1$ state, because of the complexity of the numerical treatment of the resonance radiation trapping.

II.4 Swarm parameters

To solve particle transport equations (6), it is necessary to characterize both diffusion ($\delta = 0$) and drift ($\delta = 1$) processes through swarm parameters (longitudinal and transversal diffusion coefficients as well as drift velocity and mobility (D_{L_q}, D_{T_q}, w_q and μ_q) for each type of particles. Here, ionisation and excitation coefficients by electronic impact are not considered because, in our conditions, these phenomena are very unlikely. Electron swarm parameters were calculated by directly solving Boltzmann's equation for every E/N value, knowing the collisional cross sections. The characteristic electronic energies and the drift velocity of electrons in xenon are shown in figure 7. These calculated values (for a gas temperature of $T_g = 300\,K$) concur with the compiled experimental and theoretical data **[Mat]** available in literature.

The mobility of atomic and molecular ions results from a bibliographic study **[Mat]** where different determination methods were employed (experiments and calculations) (Figure 8). For low *E/N* values experimental measurements inferred by Biondi *et al* **[Bio]** with zero field (0.58 $cm^2.V^{-1}.s^{-1}$ for the atomic state and 0.79 $cm^2.V^{-1}.s^{-1}$ for the molecular one) were used. For intermediate *E/N* values we used the data calculated by Varney *et al* **[Var]** and Oda *et al* **[Oda]** to describe the mobility of $Xe^+(^2P_{3/2})$ and $Xe_2^+(A^2\Sigma_u^+)$ ions. Finally, for high the electric fields both mobilities follow the variations proposed by Kawakami *et al* **[Kaw]**. With the constant electric field $E = 40$ $V.cm^{-1}$, *E/N* values vary between 0.24 and 4.04 $V.cm^2$ for our pressure range (30 to 500 Torr). Here, the applied uniform electric field is sufficiently low and ions can be considered to be in thermal equilibrium with the gas particles. Ionic diffusion coefficients are, as usual, deduced from the corresponding mobilities and given by the Einstein's relation:

$$\frac{D_q}{\mu_q} = \frac{k_B T_g}{e} \qquad (10)$$

where k_B is the Boltzmann constant.

As ions are much more massive than electrons, their mobilities much lower (in a ratio of 100 to 5000) and according to relation (10), ionic diffusion coefficients are much more weaker

than the electronic ones (4 to 5 orders of magnitude according to the ionic species and the gas pressure). Longitudinal and transversal diffusion coefficients of each ionic species are thus supposed to be equal (Figure 8).

For neutral excited species, we investigated about the determination of the diffusion coefficients. Concerning atomic species, the literature **[Wie]-[Bar]** only mentions the diffusion coefficient of the Xe($^3P_2$) metastable state, deduced from experimental measurements. Indeed, usually, its decay frequency τ^{-1} is expressed as a sum of different terms accounting for phenomena likely to destroy this species. To quantify these different contributions, Barbet *et al* **[Bar]** proposed to determine metastable Xe($^3P_2$) densities in an afterglow in neutral xenon from optical absorption measurements. For pressures p ranging from 0.04 to 4 Torr, the following profile was obtained:

$$\frac{1}{\tau} = \frac{19}{p.\Lambda^2} + 75p + 80p^2 \qquad (11)$$

where Λ is the characteristic diffusion length of the Xe($^3P_2$) metastable in the discharge cell. The first term of the right-hand member of equation (11) accounts for metastable diffusion towards the wall of the enclosure. The second and third terms are respectively related to 2- and 3-body collisional processes between the Xe($^3P_2$) state and one or two neutral atoms of the gas Xe($^1S_0$). Then, Barbet *et al* **[Bar]** have identified equation (11) with the general form of the decay frequency of the Xe($^3P_2$) species, given by:

$$\frac{1}{\tau} = \frac{D_0}{p.\Lambda^2} + A_1 p + A_2 p^2 \qquad (12)$$

where $D_0 = 19\ \mathrm{cm}^2.\mathrm{Torr.s}^{-1}$ is the diffusion coefficient of the Xe($^3P_2$) metastable in xenon at 1 Torr and 300 K, and A_1 and A_2 are the reaction rates of two and three body processes, respectively. As neutral species diffuse very slowly (such as ions) with time-scales around several tens of microseconds at most ($p = 30$ Torr), the same value of the longitudinal and transversal diffusion coefficients was chosen for all the populations of excited atoms. In the present work, considering the gas temperature value $T_g = 293\,K$, the variation of the diffusion coefficient of atomic excited species as a function of the pressure is finally given by:

$$D^*(p)(= D_L^* = D_T^*) = \frac{D_0}{p}\frac{293}{300} \qquad (13)$$

Not any diffusion coefficient of molecular species was found in the literature. Since the molecular states 0_u^+($^3P_1$) et 1_u($^3P_2$) are more massive than the atomic excited levels 6s, 6s' and 6p, they have lower diffusion coefficient values. So, we have considered that excimers would at most

diffuse as fast as the excited atoms. Thus, the diffusion coefficients of excited molecules have been chosen equal to those of the atomic levels (relation (13)).

Table 2 gathers the whole data on species transport for both pressures, with or without the electric field $E = 40$ V.cm^{-1}.

II.5 Numerical formulation

To perform the numerical treatment of equation (6) we used the "multi-step method" **[Yan]**. It consists in splitting the initial equation (6) in a series of simpler equations, corresponding to every operator of this equation in such a way that, for example, a multidimensional problem is transformed into a set of easier problems. Thus, equation (6) is supposed to be equivalent to the following system:

$$\frac{\partial n_q}{\partial t}(x,y,t) + \vec{\nabla}.\left[\vec{w}_q(x,y,t).n_q(x,y,t)\right] = 0 \qquad (14)$$

$$\frac{\partial n_q}{\partial t}(x,y,t) - \vec{\nabla}.\left[\overline{\overline{D}}_q(x,y,t).\vec{\nabla}n_q(x,y,t)\right] = 0 \qquad (15)$$

$$\frac{\partial n_q}{\partial t}(x,y,t) = S_q(x,y,t) \qquad (16)$$

The above equations are discretised by means of an adequate numerical approach and sequentially solved with an elementary time step Δt. The initial conditions related to every equation correspond to the solution coming from the former equation. Then, the solution of (15) is obtained by adopting the solution of (14) at the beginning of the time step. The numerical methods used were previously employed by Pancheshnyi *et al* **[Pan]**. An extensive description can be found in **[Ces]-[Cap-1]**.

III. Results and discussion

As explained earlier, our model formulation is devoted to the study of particle transport resulting from recombination in xenon after a brief (2+1) photon ionisation via the Xe($^3P_2$) relay state. The results presented in this paper cannot be really compared with experiments, where both phenomena (excitation and recombination) occur simultaneously.

To facilitate the kinetic analysis table 3 provides the characteristic times of each reaction for 30 and 500 Torr. It is important to note that for electronic recombinations (R.02 and R.03), the maximum value of the initial electronic number density is used for their estimations. Table A.1 in

the appendix summarizes all the characteristic diffusion times along the *x* and *y* directions, with or without electric field and their drift durations as well.

In this section, we base ourselves on 2D spatial distributions and 1D (along $[Cx)$ axis) profiles of particle number densities in order to describe the spatio-temporal evolutions. On the one hand, 2D representations lead to qualitative descriptions but clearly show dissymmetry between *x* and *y* directions. On the other hand, 1D profiles enable quantitative descriptions. We note that the terms "distribution" and "profile" will respectively refer to 2D and 1D spatial evolutions of number densities, whereas "temporal evolutions" is reserved for either the time-dependent of total number of particles per unit length (cm^{-1}) along *z* axis, or the VUV radiation power per unit length ($W.cm^{-1}$).

III.1 Particle and VUV emission dynamics at 30 Torr

III.1.1 Absence of electric field (E = 0 $V.cm^{-1}$)

III.1.1.1 Spatial distribution

a) Charged particle transport

Figure 9 depicts the 2D variations (in logarithmic scale) of the spatial distributions of charged particles, without electric field. All the charged particles spread outwards while their maxima number densities always remain at the centre C. Electrons and atomic ion densities collapse while molecular ion ones grow up. The ions remain confined within the laser envelope whereas electrons slightly spread outside this domain. Both ionic number densities evolve and are faster than the electronic ones, with similar time constants.

The spreading of charged species is due to physical diffusion phenomena whose time constants are given in the appendix. In addition, collisional processes occur (R.01, R.02 and R.03). Atomic ions decay mainly by reaction R.01 ($\tau_{reac}^{(1)} = 5.1\,\mu$s) to form molecular ions. In a previous work **[Cap-2]**, we showed that:

- Recombination of electrons is more likely through reaction R.03 ($\tau_{reac}^{(2)} \geq 10^5$ s and $\tau_{reac}^{(3)} \geq 94$ ms).
- Neither the electronic temperature dependence of the rate constant of molecular ion recombination nor the nature of its reaction by-products has a significant influence on the kinetics.

Figure 9 also illustrates that the extension of electron distribution is always slightly higher (about 3 %) along $[Cx)$. This is due to the values of the longitudinal ($D_{L_e} = 832\ cm^2.s^{-1}$) and

transversal ($D_{T_e} = 806\ \mathrm{cm^2.s^{-1}}$) electronic diffusion coefficients. Furthermore, ions hardly diffuse: $D_{L_{Xe^+}} = D_{T_{Xe^+}} = 0.34\ \mathrm{cm^2.s^{-1}} \approx \frac{D_{L_e}}{2000}$ and $D_{L_{Xe_2^+}} = D_{T_{Xe_2^+}} = 0.47\ \mathrm{cm^2.s^{-1}}$. Since atomic ions remain in the laser envelope, molecular ions are confined in this domain as well.

These results are consistent with figures 10.a and 11. The former shows that the electronic number density profiles remain all the time centred in the middle of the simulation domain. Initially equal to 10^7 cm^{-3}, its maximum gradually decreases: 9.8x10^6, 9.5x10^6, 9.1x10^6, 8.3x10^6 and 6.7x10^6 cm^{-3} at 2, 5, 10, 20 and 50 µs, respectively. In addition, the base of the electronic profile becomes elliptic and its major half-axis is along $[Cx)$. Concerning atomic ions, the successive maxima of $Xe^+(^2P_{3/2})$ number densities decrease (Figure 11.a) much more rapidly: 6.8x10^6, 3.8x10^6, 2.0x10^5 and 5.7 x10^2 cm^{-3} at 2, 5, 20 and 50 µs, respectively. The molecular ions number density (Figure 11.b) increases from zero to reach maxima equal to 3.2x10^6, 6.2x10^6, 9.8x10^6 and nearly 10^7 cm^{-3} at 2, 5, 20 and 50 µs, respectively.

b) Excited atomic state and excimer transport

The 2D spatial distributions of the 6p state (Figure 9) show that its number density, initially equal to zero, rises quite fastly and reaches its maximum at about 20 µs (Figure 12.a) and then vanishes much more slowly (at t = 50 µs, it is equal to 2.8x10^{-1} cm^{-3}), remaining all the time, centred on the symmetry axis of the system. Since the 6p number density is much lower than the charged particles' one, the upper limit of its scale range was chosen to match with its maximum value (Figure 12.a). At 20 and 50 µs, the atomic ion density is much lower than the molecular one (Figure 11), and consequently, the density distribution of the 6p states is merely governed by electronic and molecular ions. Indeed, Xe(6p) states are only produced by reaction R.03 and the spatial distribution of their number densities is similar to those of both electrons (Figure 10.a) and molecular ion ones (Figure 11.b). Even if electrons weakly diffuse outside the laser envelope (Figure 9), the 6p states remain confined inside this region, because no molecular ion exists outside.

The number densities of the 6p states are quite low because they are destroyed more rapidly through reactions R.04 to R.07 ($\tau_{reac}^{(4)+(5)+(6)+(7)} = 4$ ns) than they are created by reaction R.03 ($\tau_{reac}^{(3)} \geq 94$ ms). Thus, the very low amount of 6p states, at all times, suggests that once created, they mainly disappear (80 %) very rapidly ($\tau_{reac}^{(6)+(7)} = 5$ ns) by two-body collisions (reactions R.06 and R.07), and to form the $^3P_1$ resonant (49 %) and $^3P_2$ metastable (51 %) states with nearly the same ratio. Globally, the 6s states are much more rapidly generated from the 6p

states than they are consumed. This result is not surprising considering the frequencies of reactions R.08, R.09 and R.10 which only account for the loss of the 6s states. For clarity sake, 2D distributions of the excimers correlated to $Xe(^3P_1)$ are given with a same scale range whose upper limit corresponds to the maximum value of the $Xe(^3P_1)$ number density. This remark also holds for the excimers correlated to $Xe(^3P_2)$. The 2D distributions of $Xe(^3P_1)$ and $Xe(^3P_2)$ states (both initially not populated) are similar to the 6p ones and differ for their decay times and amplitudes. The excimers follow the same trends as those of the 6s states. Nevertheless, their 2D distributions are much lower (about two or three orders of magnitude).

III.1.1.2 Temporal profile

a) Charged particle number

In the absence of any electric field, the total number (truly speaking, it is the number of electrons per unit length, refer to section III.1) of electrons, initially equal to $9.2x10^4$ cm^{-1}, always remains quasi-constant (Figure 13.a). The low decrease observed is due to the few electronic collisions which produce the 6p states. Indeed, the characteristic times of the only two reactions R.01 and R.02 which enable atomic ion loss are, respectively, $\tau_{reac}^{(1)} = 5.1\,\mu s$ and $\tau_{reac}^{(2)} \geq 10^5$ s. Thus, as mentioned above, electronic recombination R.02 of atomic ions is almost nonexistent in our calculation conditions. Once created, molecular ions only disappear by electronic recombinations with a characteristic time $(\tau_{reac}^{(3)} \geq 94\ \text{ms})$ much greater than our time-range. This explains the low decrease of the density of electrons compared to atomic ion ones.

The strong decrease of the total number of ions $Xe^+(^2P_{3/2})$, quasi-exclusively governed by reaction R.01, is represented in figure 13.a@. It shows a nearly exponential decay with a time constant $\tau_{reac}^{(1)} = 5.1\,\mu s$. This decrease occurs together with an enhancement of the total number of molecular ions with the same time constant. Beyond 30 µs, the saturation of the spatial distributions of molecular ions number densities, showed by figures 9 and 11.b, is visible on this temporal profile. At all times, electro-neutrality is respected.

b) Excited atomic state number

The metastable state is more abundant than the resonant one (Figure 14.a). Indeed, the latter is consumed more rapidly $(\tau_{reac}^{(9)} = 6.3\,\mu s)$ than metastable ones by 3-body collisions $(\tau_{reac}^{(10)} = 13\,\mu s)$. In addition, they can also de-excite $(\tau_{reac}^{(8)} = 3.3\,\mu s)$ to the ground state $Xe(^1S_0)$

by emitting resonant photons. It is quite natural that $Xe(^3P_1)$ reaches its maximum before the $Xe(^3P_2)$, both of them lagging behind the Xe(6p).

To understand the temporal evolution of the total number of 6p states, we carried out an analytic resolution of the linear system of differential equations (0-D model) which describes reactions R.01 to R.07 given in table 1. In particular, we assumed that the electronic density remained constant and that diffusion phenomena were much slower than the reactions of table 1. The total number of 6p states is then given by a sum of three exponential terms:

$$N_{Xe(6p)}(t) = \alpha_1 \exp\left(-\frac{t}{\tau_1}\right) + \alpha_2 \exp\left(-\frac{t}{\tau_2}\right) + \alpha_3 \exp\left(-\frac{t}{\tau_3}\right) \qquad (17)$$

with $\tau_1 = \tau_{reac}^{(3)} \geq 94$ ms, $\tau_2 = \tau_{reac}^{(1)} = 5.1\,\mu$s and $\frac{1}{\tau_3} = \frac{1}{\tau_{reac}^{(4)}} + \frac{1}{\tau_{reac}^{(5)}} + \frac{1}{\tau_{reac}^{(6)}} + \frac{1}{\tau_{reac}^{(7)}} = \frac{1}{4\text{ ns}}$.

Thus, the evolution of the total number of 6p states, at long times, accounts for their creation by reaction R.03 (the slowest). However, the electronic number density is not constant and the diffusion times of some species are similar (Appendix) to the characteristic times of reaction R.03. So, the observed decay is not strictly exponential. This statement is also valid for the 6s states and the excimers, but they contain more exponential terms.

c) Excimer number

Figure 15a shows that the $Xe_2[0_u^+(^3P_1)]_h$ excimer is more rapidly produced but in much less extent than $Xe_2[1_u(^3P_2)]_h$. This is due to the combination of several phenomena, especially the swiftness of reaction R.09 compared to reaction R.10, and the lower lifetime of $Xe_2[0_u^+(^3P_1)]_h$ than that of $Xe_2[1_u(^3P_2)]_h$. So, once created, $Xe_2[0_u^+(^3P_1)]_h$ excimers disappear more rapidly either by emitting the first continuum (reaction R.13) or by creating the $^3P_2$ state (reaction R.15) or through vibrational relaxation to attain the $Xe_2[0_u^+(^3P_1)]_b$ level (reaction R.14). The maximum of their total number is reached at about 22 µs whereas it occurs at 45 µs for the $Xe_2[1_u(^3P_2)]_h$ states. As the $^3P_1$ levels are scarcer than the $^3P_2$ states, the excimers correlated to the resonant state follow the same trend.

d) VUV luminescence decay

Figure 16.a shows that $Xe_2[1_u(^3P_2)]_h$ mainly contributes to the emission of the first continuum. Nevertheless, at short times, the VUV radiation is more intense for $Xe_2[0_u^+(^3P_1)]_h$ than $Xe_2[1_u(^3P_2)]_h$ excimers. This is due to both the temporal profiles of the total number of $Xe(^3P_1)$ and $Xe(^3P_2)$ states and the respective lifetimes of the molecular states ($\tau_{reac}^{(11)} = 40$ ns and $\tau_{reac}^{(13)} = 5$ ns). At long times, this trend is inversed (Figure 16.a) because of the sharp

predominance of $^3P_2$ atoms over the $^3P_1$ ones (Figure 14.a). We also note that the first continuum emission is rather slow (maximum reached at about 40 µs) compared with the results, obtained elsewhere either with selective excitation (maximum reached at several nanoseconds for 60 Torr) **[Led]**, or with non-selective excitation in a mono-filamentary DBD (maximum at around 100 ns for 50 Torr) **[Sew-2]**. Moreover, in both experiments, electronic reactions are not observed. In our case, the slow component comes from electronic recombination by reaction R.03.

As expected, the emission of the second continuum (Figure 17.a) is mainly due to the contribution of $Xe_2[1_u(^3P_2)]_b$ states, since its maximum (reached at about 45 µs) more or less coincides with the $Xe_2[1_u(^3P_2)]_b$ excimers' one (Figure 16.a).

The second continuum is slightly more intense than the first one (Figure 18.a) and this is consistent with a higher population of $Xe(^3P_2)$ levels than the $Xe(^3P_1)$ ones (Figure 14.a). Indeed, according to the collision frequencies, when $Xe_2[0_u^+(^3P_1)]_h$ are populated, 68.5 % of these excimers contribute to the first continuum and the remaining leads to the second continuum. When $Xe_2[1_u(^3P_2)]_h$ states are populated, only 30 % of the emitted radiation is in the first continuum. This feature was observed elsewhere, since at 25 Torr, under selective excitation, the second continuum is more intense than the first one when only the $^3P_2$ metastable is initially excited **[Led]**, whereas it becomes clearly weaker when initial excitation is performed on the resonant $^3P_1$ level. As our calculations show that the number of metastables always remains greater than the resonant ones, this result is consistent. Anyway, in neutral xenon mono-filamentary DBDs, Sewraj *et al* **[Sew-2]** show a strong population of the $^3P_2$ states obtained even at 25 Torr.

III.1.2 Presence of electric field (E = 40 V.cm^{-1})

III.1.2.1 Particle transport (spatial distribution and temporal profile)

When a Laplacian electric field $E = 40$ V.cm^{-1} is applied, a drift phenomenon (Figure 19) of charged particles is superimposed on diffusion and kinetics. So, as the electronic number density distribution propagates, its initially circular base becomes much more rapidly elliptic than without the electric field. In this case, its major half-axis is orientated towards the $[Cy)$ direction. This result is consistent with the difference between the longitudinal ($D_{L_e} = 7.91\text{x}10^3$ cm^2.s^{-1}) and transversal ($D_{T_e} = 3.52\text{x}10^4$ cm^2.s^{-1}) diffusion coefficient values, accentuated with electric field. Besides, the electric field (Figure 10.b) enhances electronic diffusion. Indeed, at 2, 5 and 10 µs, the maximal values of electronic number densities have dropped to 6.7x10^6, 4.6x10^6 and to

$3.0x10^6$ cm^{-3}, respectively. At 20 µs, the value of this maximum of the number density (about $4.2x10^4$ cm^{-3}) has strongly decreased due to the loss of electronic charges (on the anode side). The electrons, extremely mobile, drift very rapidly ($w_e = 2.13x10^5$ $cm.s^{-1}$) towards this electrode. Indeed, the maximum of the electronic number density distribution along the $[Cx)$ axis is located at the positions x = 2.5, 2.9, 3.6 and 5 mm, respectively, at $t = 0, 2, 5$ and $10\ \mu s$ (Figure 10.b).

The $Xe^+(^2P_{3/2})$ ions number density distributions (Figure 19) are similar to those obtained without electric field (Figure 9), except that they drift extremely slowly ($w_{Xe^+} = -588\ cm.s^{-1}$) towards the cathode compared to those of electrons. With our scales (several tens of microseconds), these ions seem quasi-static whereas the electrons are very quickly collected at the anode. Indeed, since the first microseconds, the very quick drift of electrons confines these charges at the right of the $x = x_0$ plane (Figure 10.b). The electronic recombinations are then obviously predominant in this region where atomic ion should fade out, rendering its density dissymmetric. In fact, this phenomenon is imperceptible over our time scale because reaction R.02 ($\tau_{reac}^{(2)} \geq 10^5$ s) is much less likely (Table 3) than reaction R.01 ($\tau_{reac}^{(1)} = 5.1\ \mu s$). Consequently, the $Xe^+(^2P_{3/2})$ ions preferentially disappear by three body collisions (R.01) and their densities are quasi non-affected by the electronic distribution. The decrease of the atomic ions number density occurs together with the growth of the $Xe_2^+(A^2\Sigma_u^+)$ one. Its drift, which is slightly greater ($w_{Xe_2^+} = -800\ cm.s^{-1}$) than the $Xe^+(^2P_{3/2})$ ion's one, shifts more rapidly the maxima of their number densities towards the cathode. Our calculations show that the density of $Xe_2^+(A^2\Sigma_u^+)$ reaches its maximum after 30 µs **[Cap-1]**.

The electron dynamics is modified whereas the ions' one remains unchanged. Indeed, as shown in figure 13.b, from 6 µs, the total number of electrons strongly decreases non-exponentially. As already explained above, this is due to a loss of electronic charges which are collected at the anode (Figure 10.b). Yet, the decay of atomic ions remains identical to that obtained without electric field. The total number of atomic ions exponentially decreases as reaction R.02 is always almost unlikely ($\tau_{reac}^{(2)} \geq 10^5$ s), even if the electronic recombination of molecular ions ($\tau_{reac}^{(3)} \geq 885$ ms) is ten-fold faster without electric field. Because of the collected electrons, electro-neutrality is not respected anymore. Beyond 30 µs, the atomic ions have completely disappeared by three body collisions, to generate a medium whose charged particles are only molecular ions.

The Laplacian field breaks the symmetry (Figures 9 and 19) of the distribution of the 6p states number density because of the strong electronic drift towards the anode (Figure 19) and the

much slower and opposite ionic (molecular) one. It is particularly visible at 10 µs (Figure 19), where both drifts preferentially favour electronic recombination on the right of the $x = x_0$ half-plane. The subsequent distribution of the 6p states at 10 µs (Figure 19) has a partial moon-shape because only few electrons remain in the right-side of the laser envelope (Figures 19 and 10.b).

The density profiles of $Xe(^3P_1)$ and $Xe(^3P_2)$ along $[Cx)$ are naturally similar to the 6p ones (Figure 12.b), but are respectively about one hundred or one thousand times. Globally, all excited atomic state densities are weaker in the presence electric field because electrons drift on the right of the laser envelope.

Beyond 8 µs, the temporal evolutions of the lowest atomic states (Figure 14.a) and their correlated excimers (Figure 15.a) are purely exponential because electronic recombination is over. Consequently, the system of differential equations (first order) describing the reactions of table 1 becomes perfectly linear. In particular, the time constant of the slowest component of the density profile of the $Xe(^3P_1)$ and $Xe(^3P_2)$ are respectively 13 and 2.17 µs. The first time constant correspond to reaction R.10 whereas the second one is inverse of the sum of the decay frequencies of reactions R.08 and R.09. We will not further discuss this feature which also holds for molecular states since it only describes a linear system of differential equations.

The temporal evolutions of molecular states (Figure 15.a) are consistent with the separation of charged species (Figure 13.a). The low vibrational level excimers are always more populated than their corresponding high vibrational level molecules (Figure 15.a). This occurs because even at 30 Torr, once created, the high lying excimers quickly vibrationaly relax through two-body collisions (reactions R.12, R.14 and R.15). Besides, excimers correlated to the metastable states are always more abundant than those correlated to the resonant level because, as stated earlier, the metastable state is itself much more populated than the resonant one.

III.1.2.2 VUV luminescence decay

When an external electric field is applied, each VUV emission (1^{st} and 2^{nd} continua and resonant radiation) is greatly reduced (Figures 16, 17 and 18) since the excited species are less abundant. Moreover, at late times (t > 8 µs), the slow components of the decay of 1^{st} and 2^{nd} continua as well as resonant line shape no more exist, because of the severe drop of electronic density. The decay frequencies of the slowest components (at late times) are sums of the relevant decay frequencies of reactions R.08 to R.17. In figure 16.b, only the $Xe_2[1_u(^3P_2)]_h$ contribute for the 1^{st} continuum emission at long times whereas at short times, it comes from the $Xe_2[0_u^+(^3P_1)]_h$

because of the relative total number of particles of these species. For similar consideration, the 2nd continuum is mainly due to the $Xe_2[1_u(^3P_2)]_b$ at long times and $Xe_2[0_u^+(^3P_1)]_b$ at initial ones.

For the total VUV radiation (Figure 18.b), at short times, all the three emissions (1st and 2nd continua and resonant radiation) are present, with the resonance line being about three times stronger. At long times, the 2nd continuum is about twice stronger than the 1st continuum. The resonance line is negligible because the electronic recombination no more exists to populate the $^3P_1$ state. The kinetics is similar to those observed in TALIF and ThALIF experiments, where only the relaxation of the deposited energies (within the first 8 µs) is observed.

III.2 Particle and VUV emission dynamics at 500 Torr (absence of electric field)

At 500 Torr, the frequencies of collisional reactions R.01, R.06, R.07, R.09, R.10, R.12, R.14 and R.15 are significantly enhanced. Consequently, 2D distributions and 1D profiles of certain number densities are modified. Some reactions become less likely and time scales are greatly reduced. We verified that our results are consistent with the kinetic scheme, and we will only provide the temporal decays of excited species and luminescence decays in the absence of electric field, so as to illustrate the observed differences at high pressure. We remind that the diffusion times of each species are now higher (Appendix) so that the related phenomena become rather slower, whereas characteristic times (Table 3) of radiative de-excitations remain unchanged. Two- and three- body reactions are, respectively 16.7 and 278 times as much faster. The electronic recombination R.02 of atomic ions remains unlikely.

The results given in reference **[Cap-1]** show that the temporal evolution of the total number of each charged particle is very similar to figure 13.a, but with a much shorter timescale. Indeed, the total number of electrons is always nearly constant **[Cap-1]**, while the time constant for $Xe^+(^2P_{3/2})$ and $Xe_2^+(A^2\Sigma_u^+)$ is about $\tau_{reac}^{(1)} = 18$ ns, which fully agrees with reaction R.01. When $E = 40$ V.cm^{-1}, the total number of electrons remain nearly constant until 14 µs (instead of 6 µs at 30 Torr). This is due to their drift time, 5.5 times longer at 500 Torr than at 30 Torr (*cf* Appendix).

Subsequently, the 6p, 6s and molecular states are created much earlier at 500 Torr (Figure 20) than at 30 Torr (Figures 14.a and 15.a). Beyond 400 ns, the total number of each species seems constant. In fact, they all have a very slow and nearly exponential decay ($\tau_{reac}^{(3)} \geq 94$ ms). Now, low vibrational excimers are predominant (Figure 20.b). Indeed, once created, the $Xe_2[1_u(^3P_2)]_h$ and $Xe_2[0_u^+(^3P_1)]_h$ states mainly relax ($\tau_{reac}^{(12)} = \tau_{reac}^{(15)} = 1$ ns). Besides, the

transfer reaction R.15 induces further more $Xe_2[1_u(^3P_2)]_h$ which again quickly relaxes to form more $Xe_2[1_u(^3P_2)]_b$ excimers. Thus, as expected, at 500 Torr, the first continuum emission is weaker and its maximum is about 3.3 times less important than at 30 Torr (Figures 21 and 18.a). Yet, about 75 % of its intensity comes from the $Xe_2[0_u^+(^3P_1)]_h$ state. This result, apparently surprising, is not absurd if we consider the total number of VUV emitting states and their respective radiative lifetimes. According to our results, the VUV radiation of the first continuum coming from the $Xe_2[0_u^+(^3P_1)]_h$ state is 2.5 times more intense than the one related to the $Xe_2[1_u(^3P_2)]_h$ state **[Cap-1]**. This result is consistent with the ratio between the radiative lifetimes of these excimers $\left(\frac{\tau_{reac}^{(11)}}{\tau_{reac}^{(13)}} = 8\right)$ and the one of their total number $\left(\frac{N(Xe_2[1_u(^3P_2)]_h)(t)}{N(Xe_2[0_u^+(^3P_1)]_h)(t)} \approx 3.13\right)$, remaining always constant. According to the radiative lifetimes of low vibrational molecular states, the emission of the second continuum related to the $Xe_2[0_u^+(^3P_1)]_b$ states is 3 times less important than that coming from $Xe_2[1_u(^3P_2)]_b$ **[Cap-1]**, even if the latter remains predominant over the $Xe_2[0_u^+(^3P_1)]_b$ (Figure 20.b). Figure 21 shows that about 90 % of the total VUV radiation is in the second continuum. This result is certainly overestimated because $Xe_2[0_u^+(^3P_1)]_h$ states equally relax (45 %) towards $Xe_2[0_u^+(^3P_1)]_b$ and transfer to $^3P_2$ metastables. But, in fact, the former phenomenon is much less important because of the presence of the $Xe_2(2_u,2_g,1_g,0_g^-)$ dissociative states correlated to the $^3P_2$. The intensity of the first continuum represents almost 10 % of the total VUV emission. Resonance photons are hardly emitted at 500 Torr.

IV. Conclusion

This work concerns the modeling of the transport of excited and charged species created in a laser beam following (2+1) photon ionisation via the $Xe(^3P_2)$ relay state. It is meant for the spatio-temporal follow up of the species in order to estimate the real contribution of slow recombination processes on the VUV emissions of neutral xenon. Indeed, the experimental approach can only provide simultaneously the VUV radiation issuing from both initial excitation and electronic recombination. Thus, dealing with photons resulting only from recombination processes, this paper constitutes the first step of the study of VUV emissions following TALIF experiments.

The kinetic model used is well established and it implies the main species and reactions occurring in pure xenon. Most reaction rates, used, were previously experimentally determined by our team. As expected, the results given here are fully consistent with the model, which also accounts for diffusion processes. We considered pure xenon in a weakly ionised medium. The

initial state is a double Gaussian (along x and y) electronic number density centred at the laser beam axis. These charges are balanced by an identical distribution of monoatomic xenon ions. The maximum number density is $n_0 = 10^7$ cm^{-3}. At 30 Torr, in the absence of an electric field, the temporal evolutions of the VUV intensities (measurable quantities) present a slow component issuing from the recombination of molecular ions ($\tau_{reac}^{(3)} \geq 94$ ms). Nevertheless, here, we have not taken into account the initial presence of the $^3P_2$ states distributed similarly to the electrons but with different proportions. The VUV intensities coming only from these initial metastables, certainly faster, would be much more intense and would mask the VUV intensities coming from the electronic recombination. This incomplete study, yet enables us to emphasize the slow phenomena related to electronic recombination. Considering the extremely weak number of atomic and molecular states issuing from these recombinations, we can assert that these reactions will not affect the VUV emission intensities directly coming from the initial $^3P_2$ states, in our normal conditions of selective excitation.

The temporal evolution trends of the VUV intensities are consistent with recent experimental measurements. However, some discrepancies related to the slow decay frequencies still persist. Especially, at long times, the luminescence decays obtained by calculations at 500 Torr, remain slightly slower than the measured VUV intensities **[Rod]**. The slow phenomena are related to electron recombination whose frequency depends on the electronic number density. An improvement consists in introducing an initial electronic number density which accounts for both the laser beam energy, the gas pressure, the 2-photons excitation of Xe($^3P_2$) and 1-photon ionisation cross section of this state. The reaction rates of the recombination processes are under investigation.

Nevertheless, this work allowed us to validate our approach and it enables us to follow only the contribution of recombination on VUV emissions. In order to make a direct comparison to the experiment, it will be necessary to:

- take an initial realistic distribution of the metastable number density into account, as explained formerly,
- consider a realistic initial electron density, as stated earlier,
- improve the kinetic scheme by introducing the dissociative state correlated to the $^3P_2$ metastable, whose decay frequency is very high,
- consider the spectral dependence of each group of photons and to perform a specific treatment of the radiation trapping of the resonant level, particularly to quantify the contribution of the $^3P_1$ states to the total VUV luminescence, with accuracy.

Acknowledgments

The authors would like to thank Dr. S. Pancheshnyi for his help in the realization of the movies (provided in addition of this paper) and Pr. P. Millet for helpful discussions about kinetics.

Appendix. Diffusion and drift characteristic times of the species

We here present the longitudinal and transversal characteristic times of each considered species q, along x and y respectively, defined by:

$$\tau_{diff,x,q} = \frac{D^2}{8D_{L_q}} \tag{A.1}$$

$$\tau_{diff,y,q} = \frac{L^2}{8D_{T_q}} \tag{A.2}$$

With an electric field, the drift characteristic time of each charged particle is given by:

$$\tau_{conv,q} = \frac{D}{2w_q} \tag{A.3}$$

All the values obtained at 500 and 30 Torr are gathered in table A.1.

Table 1.

Chemical reaction	Number	Reference
Molecular ion formation $Xe^+(^2P_{3/2}) + 2\,Xe(^1S_0) \xrightarrow{2\times10^{-31}\ cm^6s^{-1}} Xe_2^+(A\,^2\Sigma_u^+) + Xe(^1S_0)$	R.01	**[Mil-2]**
Electronic recombination $Xe^+(^2P_{3/2}) + e^- \xrightarrow{10^{-12}\ cm^3s^{-1}} Xe(6p)$	R.02	**[Mil-2]**
Electronic recombination $Xe_2^+(A\,^2\Sigma_u^+) + e^- \xrightarrow{1.027\times10^{-6}(\bar{\varepsilon}_g/\bar{\varepsilon}_e)^{1/2}\ cm^3s^{-1}} Xe(6p) + Xe(^1S_0)$	R.03	**[Oda]-[Osk]**
Radiative decay of Xe(6p) $Xe(6p) \xrightarrow{3x10^7\ s^{-1}} Xe(^3P_2) + h\nu_{IR}$	R.04	**[Rad]**
Radiative decay of Xe(6p) $Xe(6p) \xrightarrow{2.5x10^7\ s^{-1}} Xe(^3P_1) + h\nu_{IR}$	R.05	**[Rad]**
Collisional decay of Xe(6p) $Xe(6p) + Xe(^1S_0) \xrightarrow{10.1x10^{-11}\ cm^3s^{-1}} Xe(^3P_2) + Xe(^1S_0) + h\nu_{IR}$	R.06	**[Alf]**
Collisional decay of Xe(6p) $Xe(6p) + Xe(^1S_0) \xrightarrow{10.1x10^{-11}\ cm^3s^{-1}} Xe(^3P_1) + Xe(^1S_0) + h\nu_{IR}$	R.07	**[Alf]**
Resonance radiation decay $Xe(^3P_1) \xrightarrow{3x10^5\ s^{-1}} Xe(^1S_0) + h\nu_{res}$	R.08	**[Mar-2]**
High vibrational levels excimers formation $Xe(^3P_1) + 2Xe(^1S_0) \xrightarrow{1.63x10^{-31}\ cm^6s^{-1}} Xe_2[0_u^+(^3P_1)]_h + Xe(^1S_0)$	R.09	**[Led]**
High vibrational levels excimers formation $Xe(^3P_2) + 2Xe(^1S_0) \xrightarrow{7.87x10^{-32}\ cm^6s^{-1}} Xe_2[1_u(^3P_2)]_h + Xe(^1S_0)$	R.10	**[Led]**
Radiative decays of excimer $Xe_2[1_u(^3P_2)]_h \xrightarrow{2.5x10^7\ s^{-1}} 2Xe(^1S_0) + h\nu_{1c}$	R.11	**[Mad]**
2-body collisional relaxation of high levels excimers $Xe_2[1_u(^3P_2)]_h + Xe(^1S_0) \xrightarrow{6.09x10^{-11}\ cm^3s^{-1}} Xe_2[1_u(^3P_2)]_b + Xe(^1S_0)$	R.12	**[Bon]**
Radiative decays of excimer $Xe_2[0_u^+(^3P_1)]_h \xrightarrow{2x10^8\ s^{-1}} 2Xe(^1S_0) + h\nu_{1c}$	R.13	**[Bon]**
2-body collisional relaxation of high levels excimers $Xe_2[0_u^+(^3P_1)]_h + Xe(^1S_0) \xrightarrow{6.09x10^{11}\ cm^3s^{-1}} Xe_2[0_u^+(^3P_1)]_b + Xe(^1S_0)$	R.14	**[Bon]**
$Xe(^3P_2)$ formation via crossing of potential curves and fast molecular dissociation $Xe_2[0_u^+(^3P_1)]_h + Xe(^1S_0) \xrightarrow{6.09x10^{-11}\ cm^3s^{-1}} Xe(^3P_2) + 2Xe(^1S_0)$	R.15	**[Bon]**
Radiative decays of excimer $Xe_2[1_u(^3P_2)]_b \xrightarrow{9.71x10^6\ s^{-1}} 2Xe(^1S_0) + h\nu_{2c}$	R.16	**[Led]**
Radiative decays of excimer $Xe_2[0_u^+(^3P_1)]_b \xrightarrow{2.5x10^7\ s^{-1}} 2Xe(^1S_0) + h\nu_{2c}$	R.17	**[Ket]**

Table 2.

		p = 30 Torr		p = 500 Torr	
N (cm^{-3})		$9.88.10^{17}$		$1.65.10^{19}$	
		Without electric field	With electric field	Without electric field	With electric field
E/N (Td)		0.00	4.04	0	0.24
e^-	μ_e ($cm^2.V^{-1}.s^{-1}$)	$3.42x10^4$	$5.33x10^3$	$2.05x10^3$	$2.36x10^3$
	w_e ($cm.s^{-1}$)	0.00	$2.13x10^5$	0.00	$9.43x10^4$
	D_{L_e} ($cm^2.s^{-1}$)	$8.32x10^2$	$7.91x10^3$	$4.99x10^1$	$5.32x10^2$
	D_{T_e} ($cm^2.s^{-1}$)	$8.06x10^2$	$3.52x10^4$	$4.83x10^1$	$5.08x10^3$
$Xe^+(^2P_{3/2})$	μ_{Xe^+} ($cm^2.V^{-1}.s^{-1}$)	$1.47x10^1$	$1.47x10^1$	$8.80x10^{-1}$	$8.80x10^{-1}$
	w_{Xe^+} ($cm.s^{-1}$)	0.00	$-5.88x10^2$	0.00	$-3.53x10^1$
	$D_{L_{Xe^+}} = D_{T_{Xe^+}}$ ($cm^2.s^{-1}$)	$3.40x10^{-1}$	$3.40x10^{-1}$	$2.08x10^{-2}$	$2.08x10^{-2}$
$Xe_2^+(A^2\Sigma_u^+)$	$\mu_{Xe_2^+}$ ($cm^2.V^{-1}.s^{-1}$)	$2.00x10^1$	$2.00x10^1$	1.20	1.20
	$w_{Xe_2^+}$ ($cm.s^{-1}$)	0.00	$-8.00x10^2$	0.00	$-4.80x10^1$
	$D_{L_{Xe_2^+}} = D_{T_{Xe_2^+}}$ ($cm^2.s^{-1}$)	$4.70x10^{-1}$	$4.70x10^{-1}$	$2.80x10^{-2}$	$2.80x10^{-2}$
6p, $^3P_2$ and $^3P_1$ states	$D_{L_{Xe^*}} = D_{T_{Xe^*}}$ ($cm^2.s^{-1}$)	$6.19x10^{-1}$	$6.19x10^{-1}$	$3.71x10^{-2}$	$3.71x10^{-2}$
$1_u(^3P_2)$ $0_u^+(^3P_1)$ states	$D_{L_{Xe_2^*}} = D_{T_{Xe_2^*}}$ ($cm^2.s^{-1}$)	$6.19x10^{-1}$	$6.19x10^{-1}$	$3.71x10^{-2}$	$3.71x10^{-2}$

Table 3.

Chemical reactions		Characteristic time of reaction $\tau_{reac}^{(R)}$	
		p = 30 Torr	p = 500 Torr
R.01		5.1 μs	18 ns
R.02		≥ 10^5 s	
R.03	Without field	≥ 94 ms	
	With field	≥ 885 ms	≥ 524 ms
R.04		33 ns	
R.05		40 ns	
R.06		10 ns	0.6 ns
R.07		10 ns	0.6 ns
R.08		3.3 μs	
R.09		6.3 μs	23 ns
R.10		13 μs	47 ns
R.11		40 ns	
R.12		17 ns	1 ns
R.13		5 ns	
R.14		17 ns	1 ns
R.15		17 ns	1 ns
R.16		103 ns	
R.17		40 ns	

Table A.1.

	p = 500 Torr					p = 30 Torr				
	Without electric field		With electric field			Without electric field		With electric field		
	$\tau_{diff,x}$ (s)	$\tau_{diff,y}$ (s)	$\tau_{diff,x}$ (s)	$\tau_{diff,y}$ (s)	τ_{conv} (s)	$\tau_{diff,x}$ (s)	$\tau_{diff,y}$ (s)	$\tau_{diff,x}$ (s)	$\tau_{diff,y}$ (s)	τ_{conv} (s)
e^-	63×10^{-5}	58×10^{-5}	58×10^{-6}	55×10^{-6}	6.6×10^{-6}	38×10^{-6}	0.35×10^{-3}	4.0×10^{-6}	8.0×10^{-6}	1.2×10^{-6}
$Xe^+(^2P_{3/2})$	1.5	14	1.5	14	0.71×10^{-3}	89×10^{-3}	0.80	92×10^{-3}	0.83	420×10^{-9}
$Xe_2^+(A^2\Sigma_u^+)$	1.1	10	1.1	10	0.52×10^{-3}	66×10^{-3}	0.60	66×10^{-3}	0.60	0.31×10^{-3}
$Xe(^3P_2)$	0.84	7.6	0.84	7.6	X	50×10^{-3}	0.45	0.50	0.45	X
$Xe(^3P_1)$	0.84	7.6	0.84	7.6	X	50×10^{-3}	0.45	0.50	0.45	X
Xe(6p)	0.84	7.6	0.84	7.6	X	50×10^{-3}	0.45	0.50	0.45	X
$Xe_2[1_u(^3P_2)]_h$	0.84	7.6	0.84	7.6	X	50×10^{-3}	0.45	0.50	0.45	X
$Xe_2[1_u(^3P_2)]_b$	0.84	7.6	0.84	7.6	X	50×10^{-3}	0.45	0.50	0.45	X
$Xe_2[0_u^+(^3P_1)]_h$	0.84	7.6	0.84	7.6	X	50×10^{-3}	0.45	0.50	0.45	X
$Xe_2[0_u^+(^3P_1)]_b$	0.84	7.6	0.84	7.6	X	50×10^{-3}	0.45	0.50	0.45	X

Table 1. Reactions used in xenon for particle transport modeling.

Table 2. Swarm parameters of the selected species in neutral xenon with or without electric field E = 40 V.cm^{-1}.

Table 3. Characteristic times of reactions used in our model, at 30 and 500 Torr.

Table A.1. Diffusion and drift characteristic times of species considered in neutral xenon for particle transport modeling, at 500 and 30 Torr.

References

[Alf] Alford W. J. (1992), State-to-state rate constants for quenching of xenon 6p levels by rare gases, *J. Chem. Phys., vol. 96, n° 6, p. 4330-4340.*

[Bar] Barbet A., Sadeghi N. and Pebay-Peyroula J. C. (1975), Decay of metastable xenon atoms $Xe^{*}(^{3}P_{2})$ in a xenon afterglow, *J. Phys. B.: Atom. Molec. Phys., vol. 8, n° 10, p. 1776-1784.*

[Ber-1] Bergonzo P., Patel I., Boyd W. and Kogelschatz U. (1992), Development of a novel large area excimer lamp for direct photo deposition of thin films, *Appl. Surf. Sci., vol. 54, p. 424-429.*

[Ber-2] Berejny P., Millet P., Saissac N. and Salamero Y. (1993), Spectroscopic and kinetic study of xenon after a multiphotonic excitation of the $5d\left|5/2\right|_{J=3}$ and $5d\left|7/2\right|_{J=3}$ states, *J. Phys. B: At. Mol. Opt. Phys., vol. 26, p. 3339-3353.*

[Bio] Biondi M. A. and Chanin L. M. (1954), Mobilities of atomic and molecular ions in the noble gases, *Phys. Rev., vol. 94, n° 4, p. 910-916.*

[Bon] Bonifield T. D., Rambow F. H. K., Walters G. K., McKusker M. V., Lotrents D. C. and Gutcheck R. A. (1980), Time resolved spectroscopy of xenon excimers excited by synchrotron, *J. Chem. Phys., vol. 72, p. 2914-2924.*

[Buc] Buck K., Pedraza . A. J., Benson R. S., and Park J. W. (1998), VUV-light-induced deposited silica films, *Nucl. Instrum. Methods Phys. Res. B, vol. 141, p. 675-678.*

[Cap-1] Capeillère J. (2009), Modélisations numériques bidimensionnelles du transport des particules et photons dans des gaz ionisés. Application au xénon sous excitation laser et à la propagation d'une décharge monofilamentaire à barrières diélectriques dans l'azote, *Thèse de doctorat de l'Université de Toulouse - Toulouse III, Paul Sabatier.*

[Cap-2] Capeillère J., Ségur P., Bordage M-C. and Sewraj N. (2008), 2-D numerical modeling of charged particles transport in a laser beam in neutral xenon, *Proceedings of the 19th European Conference on The Atomic and Molecular Physics of Ionized Gases, Granada, Spain, July 15-19, 2008.*

[Ces] Cesses Y. (2004), Modélisation bidimensionnelle d'une décharge à barrières diélectriques: mise en évidence de l'importance des phénomènes aux électrodes, *Thèse de doctorat de l'Université Paul Sabatier, Toulouse III.*

[Ech] Echigo S., Yamada Y., Kawanishi S., Matsui S. and Shishida K. (1996), Comparison between O_3/VUV, VUV and O_3 processes for the decomposition of organophosphoric acid triesters, *Water Sci. Technol., vol. 34, n° 9, p.81-88.*

[Eli] Eliasson B. and Kogelchatz U. (1988), UV excimer radiation from dielectric-barrier discharges, *Appl. Phys. B: Photophys. Laser Chem., vol. 46, p. 299-303.*

[Esr] Esrom H. and Kogelschatz U. (1992), Metal deposition with a windowless VUV excimer source, *Appl. Surf. Sci., vol. 54, p. 440-444.*

[Hit] Hitzschke L. and Vollkommer F. (2001), Product Families Based on Dielectric Barrier Discharges, 9th International Symposium on the Sci. Technol. of Light Sources, Ithaca, NY, August 2001, edited by Rolf S. Bergman, p. 411–421.

[Hol-1] Holstein T. (1947), Imprisonment of Resonance Radiation in Gases, *Phys. Rev., vol. 72, n° 12, p. 1212-1233.*

[Hol-2] Holstein T. (1951), Imprisonment of Resonance Radiation in Gases. II, *Phys. Rev., vol. 83, n° 6, p. 1159-1168.*

[Jon] Jonin C. and Spiegelmann F. (2002), Pseudopotential hole-particle formalism for excitations in xenon molecules and clusters. II. the electronic structure of Xe_2^*, *J. Chem. Phys., vol. 117, p. 3059-3073.*

[Kaw] Kawakami R., Okuda S., Miyazaki T. and Ikuta N. (1996), Variation of reduced mobilities of ions in gases under 12-4 potentials, *J. Phys. Soc. Jpn., vol. 65, p. 1270-1276.*

[Ket] Keto J., Gleason R. E., Bonifield Jr T. D., Walters G. K. and Soley F. (1976), Collisional mixing of the lowest bound molecular states in xenon and argon *Chem. Phys. Lett., vol. 42, n° 1, p. 125-128.*

[Kog-1] Kogelschatz U. (1990), Silent discharges for the generation of ultraviolet and vaccum ultraviolet excimer radiation, *Pure Appl. Chem., vol. 62, p. 1667-1674.*

[Kog-2] Kogelschatz U., Esrom H., Zhang J. Y. and Boyd I. W. (2000), High-intensity sources of incoherent UV and VUV excimer radiation for low-temperature materials processing, *Appl. Surf. Sci., vol. 168, p. 29-36.*

[Led] Ledru G., Marchal F., Sewraj N., Salamero Y., and Millet P. (2006), Comparative study of the formation and decay of xenon excimers following selective excitation of the $5p^5 6s$ states: spectroscopic and kinetic analysis, *J. Phys. B: At. Mol. Opt. Phys., vol. 39, p. 2031-2057.*

[Lun] Lungu C. P., Lungu A. M., Inoue G., Sakai Y. and Suguwara H. (1998), A Study on NO_2 Decomposition in a Low-Pressure Plasma and 172 nm Xenon Excimer Lamp Radiation, *Proceedings of the 4th International Conference on Reactive Plasmas, 16th Symposium on Plasma Processing and 51st Annual Gaseous Electronics Conference, October 19-23, Maui, Hawaii, USA, p.283-284.*

[Mad] Madej A. A. and Stoicheff B. P. (1988), Vacuum-ultraviolet laser spectroscopy: Radiative lifetimes of A_{1u} states of Ar_2, Kr_2, Xe_2, and dependence on internuclear distance, *Phys. Rev. A, vol. 38, n° 7, p. 3456-3466.*

[Mar-1] Marchal F., Berejny P., Sewraj N., Salamero Y. and Millet P. (2004), Energy transfers in Kr-Xe mixtures following selective multiphotonic excitation of $Kr(^3P_1)$. Temporal analysis in Kr-Xe mixtures, *J. Phys. B: At. Mol. Opt. Phys., vol. 37, p. 1279-1304.*

[Mat] Mathy N. (2004), Détermination des données pour la modélisation numérique d'une décharge électrique contrôlée par barrières diélectriques fonctionnant à la pression atmosphérique dans le xénon, *Rapport de stage de DEA Rayonnements et Imagerie en Médecine, Université Paul Sabatier, Toulouse III.*

[Mer-1] Merbahi N., Ledru G., Sewraj N. and Marchal F. (2007), Electrical behaviour and vacuum ultraviolet efficiency of monofilamentary xenon, *J. Appl. Phys., vol. 101, p. 123309-1-123309-9.*

[Mer-2] Merbahi N., Sewraj N., Marchal F., Salamero Y. and Millet P. (2004), Luminescence of argon in a spatially stabilized mono-filamentary dielectric barrier micro-discharge: spectroscopic and kinetic analysis, *J. Phys. D: Appl. Phys., vol. 37, p. 1664-1678.*

[Mer-3] Merbahi N., Sewraj N., Marchal F. Jabbour G. and Gardou J. P. (2009), Pressure dependence of a pure krypton mono-filamentary dielectric barrier discharge, *Proceedings of the 17th International Colloquium on Plasma Processes, Marseille, France, June 22-26, 2009.*

[Mil-1] Mildren R. P. and Carman R. J. (2001), Enhanced performance of a dielectric barrier discharge lamp using short-pulsed excitation, *J. Phys. D: Appl. Phys., vol. 34, n° 1, p. L1-L6.*

[Mol] Molisch A. and Oehrig B. (1998), Radiation Trapping in Atomic Vapors, Oxford Scientific Publications, Oxford: Clarendon.

[Moo] Moore C. E. (1958), Atomic Energy Levels, Natl. Bur. Stand. (US) Circ, *vol. 3, n° 467.*

[Oda] Oda A., Sakai Y., Akashi H. and Sugawara H. (1999), One-dimensional modelling of low-frequency and high-pressure Xe barrier discharges for the design of excimer lamps, *J. Phys. D: Appl. Phys., vol. 32, p. 2726-2736.*

[Osk] Oskam H. J. and Mittelstadt V. R. (1963), Recombination Coefficient of Molecular Rare-Gas Ions, *Phys. Rev., vol.132, n° 4, p. 1445-1454.*

[Pan] Pancheshnyi S., Ségur P., Capeillère J., Bourdon A. (2008), Numerical simulation of filamentary discharges with parallel adaptative mesh refinement, *J. Comp. Phys., vol. 227, p. 6574-6590.*

[Pay-1] Payne M. G. and Cook J. D. (1970), Transport of Resonance Radiation in an Infinite Cylinder, *Phys. Rev. A., vol. 2, n° 4, p. 1238-1248.*

[Pay-2] Payne M. G., Talmage J. E., Hurst G. S., and E. B. Wagner (1974), Transport of Resonance Radiation in an Infinite Cylinder, *Phys. Rev. A., vol. 9, n° 3, p. 1050-1069.*

[Pot] Potin J. (2001), Modélisation numérique d'une décharge filamentaire contrôlée par barrières diélectriques dans l'azote à la pression atmosphérique, *Thèse de doctorat de l'Université Paul Sabatier, Toulouse III.*

[Rai] Raizer Y. P. (1991), Gas Discharge Physics, Sprinter-Verlag, Berlin-Heidelberg-New York-London-Paris.

[Rad] Radzig A. A. and Sminov B. M. (1985), Springer series in Chemical Physics 31, Springer-Verlag, Berlin- Heidelberg-New York-Tokyo.

[Rod] Rodriguez Akerreta P., Jabbour G., Marchal F., Sewraj N. and Ledru G. (2008), Study of the dissociative recombination in xenon following (2+1) multiphoton ionisation, *Proceedings of the 17th International Conference on Gas Discharges and Their Applications, Cardiff, United Kingdom, September 7-12, p. 553-556.*

[Sal] Salamero Y., Birot A., Brunet H., Galy J. and Millet P. (1984), Kinetic study of the VUV xenon emissions using selective multiphoton excitation, *J. Chem. Phys., Vol. 80, p. 4774-4780.*

[Sew-1] Sewraj N., Gardou J. P., Salamero Y., and Millet P. (2000), Radiation trapping of the $^3P_1$-$^1S_0$ resonant transitions of xenon and krypton in Xe-Kr, Xe-Ar, and Kr-Ar mixtures: Kinetic analysis and determination of the Van der Waals broadening coefficients, *Phys. Rev. A, vol. 62, p. 052721-1-052721-21.*

[Sew-2] Sewraj N., Merbahi N., Gardou J. P., and Ledru G. (2009), VUV spectroscopy and post-excitation kinetic analysis of a pure xenon mono-filamentary dielectric barrier discharge (MF-DBD), *J. Phys. D.: Appl. Phys., vol. 42, p. 1-13.*

[Shi] Shiu Y. J., Biondi M. A. and Sipler D. P. (1977), Dissociative recombination in xenon: Variation of the total rate coefficient and excited-state production with electron temperature, *Phys. Rev. A, vol. 15, n° 2, p. 494-498.*

[Sos] Sosnin E. A., Stoffels E., Erofeev M. V., Kieft I. E. and Kunts S. E. (2004), The effects of UV irradiation and gas plasma treatment on living mammalian cells and bacteria: a comparative approach, *IEEE Trans. Plasma Sci., vol. 32, n° 4, p. 1544-1550.*

[Tra] Trampert K. E., Daub H. P., Neiger M., and Heering W. (2004), Novel-Hg free, flat and large Excimer lamps operated by an adaptative pulse gear, *Proceedings of the 10th International Symposium on the Science and Technology of Light Sources, Toulouse, France, August 2004, p. 509-510.*

[Var] Varney R. N. (1952), Drift velocities of ions in krypton and xenon, *Phys. Rev., vol. 88, p. 362-364.*

[Vol] Vollkommer F. and Hitzschke L. (1996), Pulsed dielectric barrier discharges-a breakthrough in UV radiation generation, *IEEE Conf. Record of 23rd Int. Conf. on Plasma Science (ICOPS) (Boston, MA) (New York: IEEE), p 270.*

[Wie] Wieme W. (1974), Decay of excited species in the afterglow of a pulsed discharge in xenon, *J. Phys. B.: Atom. Molec. Phys., vol. 7, n° 7, p. 850-856.*

[Xu] Xu X. (2001), Dielectric barrier discharge properties and applications, *Thin solid films, vol. 309, n° 1-2, p. 237-242.*

[Yan] Yanenko N. N. (1968), Méthode à pas fractionnaires. Résolutions de problèmes polydimensionnels de physique mathématique, Armand Colin, Paris.

[Zha] Zhang J-Y. and Boyd I. W. (1996), Efficient excimer ultraviolet sources from a dielectric barrier discharge in rare-gas/halogen mixtures, *J. Appl. Phys., vol. 80, p. 633-638.*

Figure 1. Cartesian geometry used to describe the experimental situation with the axial laser beam crossing between metallic electrodes.
a. Most general experimental configuration
b. Simplified configuration used for calculations

Figure 2. Schematic diagram for (2+1) ionisation of a xenon atom with two-photon resonance process via the $Xe(^3P_2)$ metastable state.

Figure 3. Initial distribution chosen for electronic density $n_{0e}(x,y)\big|_{t=0}$ as well as for atomic ions one $n_{0\,Xe^+}(x,y)\big|_{t=0}$.
a. Volume distribution
b. Projection in any (x,y) plane
c. Section in the $y = y_0$ plane
d. Section in the $x = x_0$ plane

Figure 4. Potential curves of the chosen xenon excimers **[Jon]**.

Figure 5. Mean electron energy in xenon, calculated by solving Boltzmann's equation.

Figure 6. Kinetic scheme used for particle transport modeling in xenon.

Figure 7. Electronic characteristic energies (D_{Le}/μ_e, D_{Te}/μ_e) and electron drift velocity w_e in xenon as a function of the reduced electric field E/N, calculated by solving the Boltzmann equation.

Figure 8. Variation of the product of the mobilities and longitudinal and transversal diffusion coefficients of $Xe^+(^2P_{3/2})$ and $Xe_2^+(A^2\Sigma_u^+)$ ions with the neutral gas density in pure xenon.

Figure 9. Spatial variations of the electronic, atomic ions, and 6p states number densities at 30 Torr (E = 0 V.cm^{-1}) at different times (t = 0, 20 and 50 µs). Dashed circle represents the laser envelope (logarithmic scale). Range: [1; 10^7] cm^{-3} for charged particles, [3.4x10^{-8}; 3.4x10^{-1}] cm^{-3} for 6p states.

Figure 10. Evolution of the electronic number density at 30 Torr along x in the $y = y_0$ plane at different moments of the time: **a.** without electric field **b.** with electric field.

Figure 11. Evolution of the ions number density at 30 Torr along x in the $y = y_0$ plane without electric field at different moments of the time: **a.** $Xe^+(^2P_{3/2})$ **b.** $Xe_2^+(A^2\Sigma_u^+)$.

Figure 12. Evolution of the 6p number density at 30 Torr along $[Cx)$, **a.** without field **b.** with electric field.

Figure 13. Temporal evolution of the total number of electrons, atomic ions and molecular ions, per unit length along z at 30 Torr **a.** without electric field **b.** with electric field.

Figure 14. Temporal evolution of the total number of Xe(6p) and Xe(6s) states, per unit length along z
at 30 Torr: **a.** without electric field **b.** without electric field.

Figure 15. Temporal evolution of the total number of $Xe_2[1_u(^3P_2)]_h$, $Xe_2[0_u^+(^3P_1)]_h$, $Xe_2[1_u(^3P_2)]_b$ and $Xe_2[0_u^+(^3P_1)]_b$ states, per unit length along *z* at 30 Torr: **a.** without electric field **b.** with electric field.

Figure 19. Temporal evolution of the VUV intensity of the 1st continuum and of its contributions, per unit length along *z* at 30 Torr: **a.** without field **b.** with electric field.

Figure 17. Temporal evolution of the VUV intensity of the 2nd continuum and of its contributions, per unit length along *z* at 30 Torr: **a.** without field **b.** with electric field.

Figure 18. Temporal evolution of the total VUV intensity and of its contributions from resonant states, the 1st continuum and the 2nd continuum, per unit length along *z* at 30 Torr: **a.** without field **b.** with electric field.

Figure 19. Spatial variations of the electronic, atomic ions, and 6p states number densities at 30 Torr (E = 40 V.cm^{-1}) at different times (t = 0, 10 and 20 µs). Dashed circle represents the laser envelope (logarithmic scale). Range: [1; 10^7] cm^{-3} for charged particles, [7.6x10^{-10}; 7.6x10^{-3}] cm^{-3} for 6p states.

Figure 20. Temporal evolution of the total number of excited species, per unit length along *z* at 500 Torr without electric field: **a.** 6s and 6p states **b.** excimers.

Figure 21. Temporal evolution of the contributions to the total VUV intensity, per unit length along *z* at 500 Torr, without electric field.

Figure 1.

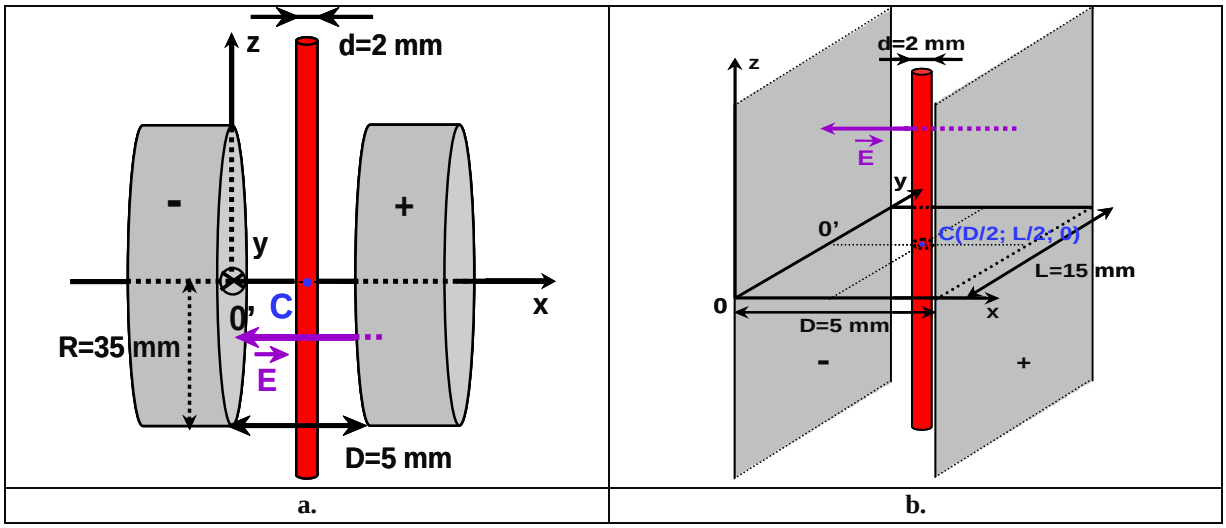

a. b.

Figure 2.

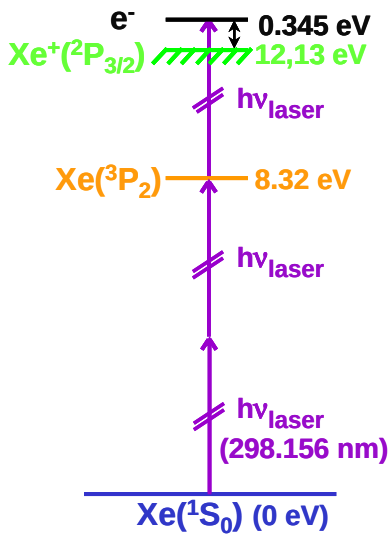
e-
0.345 eV
Xe+(2P3/2)
12,13 eV
hνlaser
Xe(3P2)
8.32 eV
hνlaser
hνlaser
(298.156 nm)
Xe(1S0) (0 eV)

Figure 3.

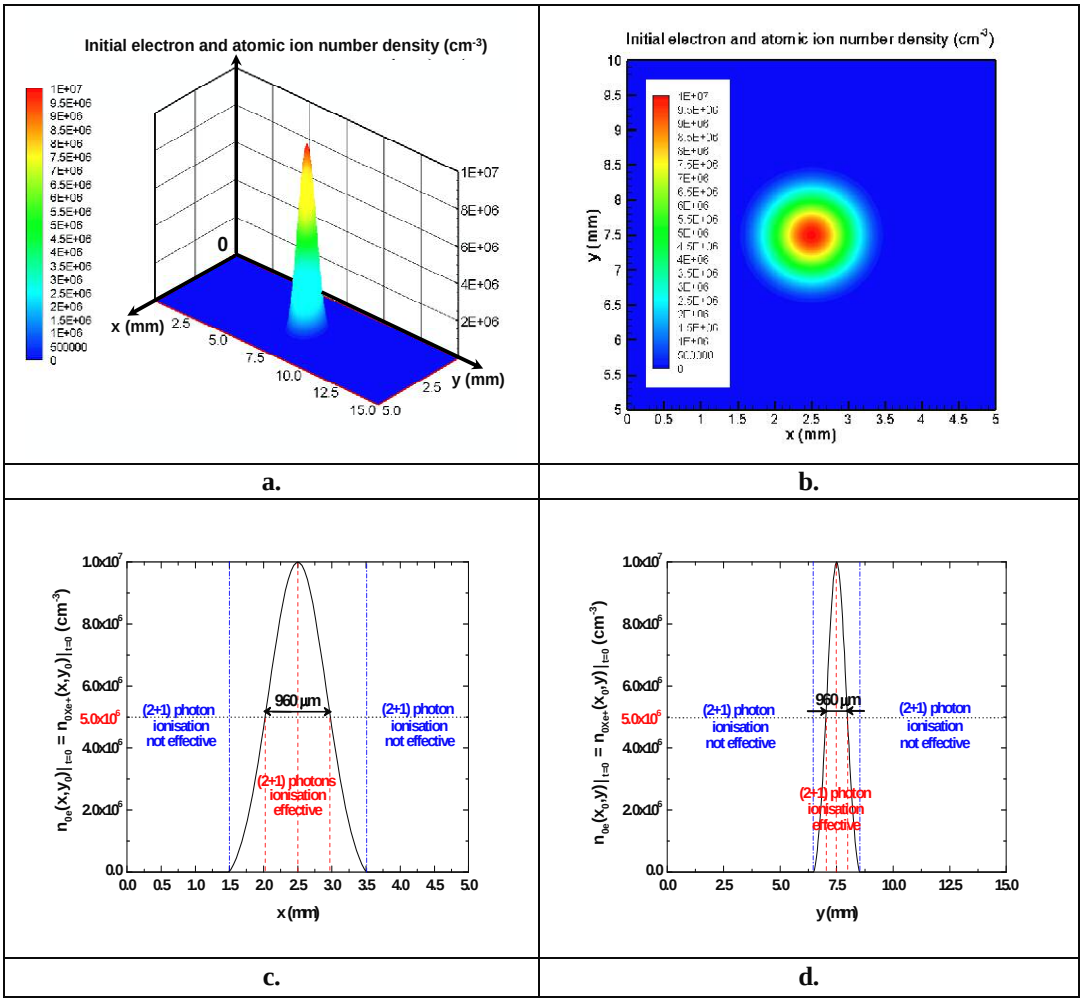
Initial electron and atomic ion number density (cm-3)
x (mm)
y (mm)
a.
Initial electron and atomic ion number density (cm-3)
y (mm)
x (mm)
b.
960 µm
(2+1) photon ionisation not effective
(2+1) photons ionisation effective
x (mm)
c.
960 µm
(2+1) photon ionisation not effective
(2+1) photon ionisation effective
y (mm)
d.

Figure 4.

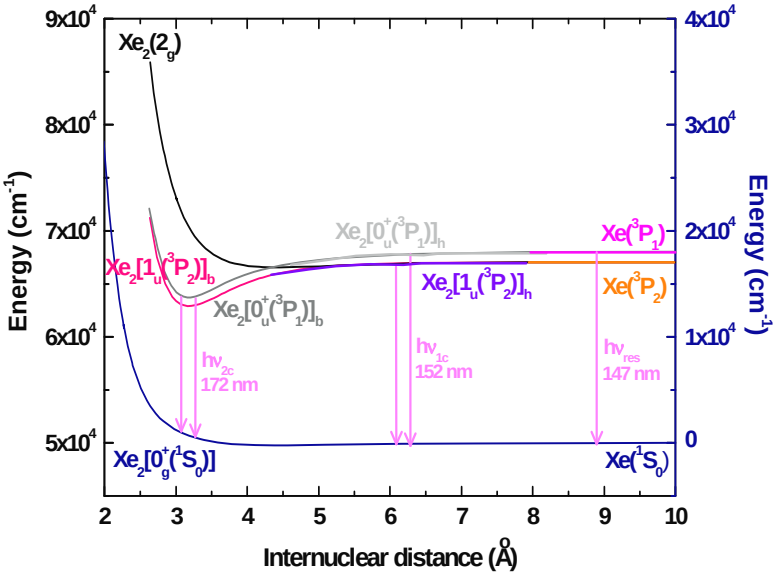
9x10^4
8x10^4
7x10^4
6x10^4
5x10^4
4x10^4
3x10^4
2x10^4
1x10^4
0
Energy (cm^-1)
Energy (cm^-1)
2
3
4
5
6
7
8
9
10
Internuclear distance (Å)
Xe2(2g)
Xe2[0u+(3P1)]h
Xe(3P1)
Xe2[1u(3P2)]b
Xe2[1u(3P2)]h
Xe(3P2)
Xe2[0u+(3P1)]b
hν2c
172 nm
hν1c
152 nm
hνres
147 nm
Xe2[0g+(1S0)]
Xe(1S0)

Figure 5.

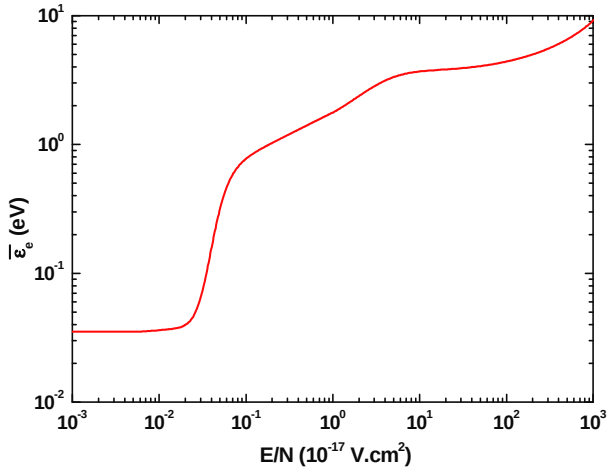
10^{1}
10^{0}
10^{-1}
10^{-2}
$\overline{\varepsilon}_e$ (eV)
10^{-3}
10^{-2}
10^{-1}
10^{0}
10^{1}
10^{2}
10^{3}
E/N (10^{-17} V.cm^2)

Figure 6.

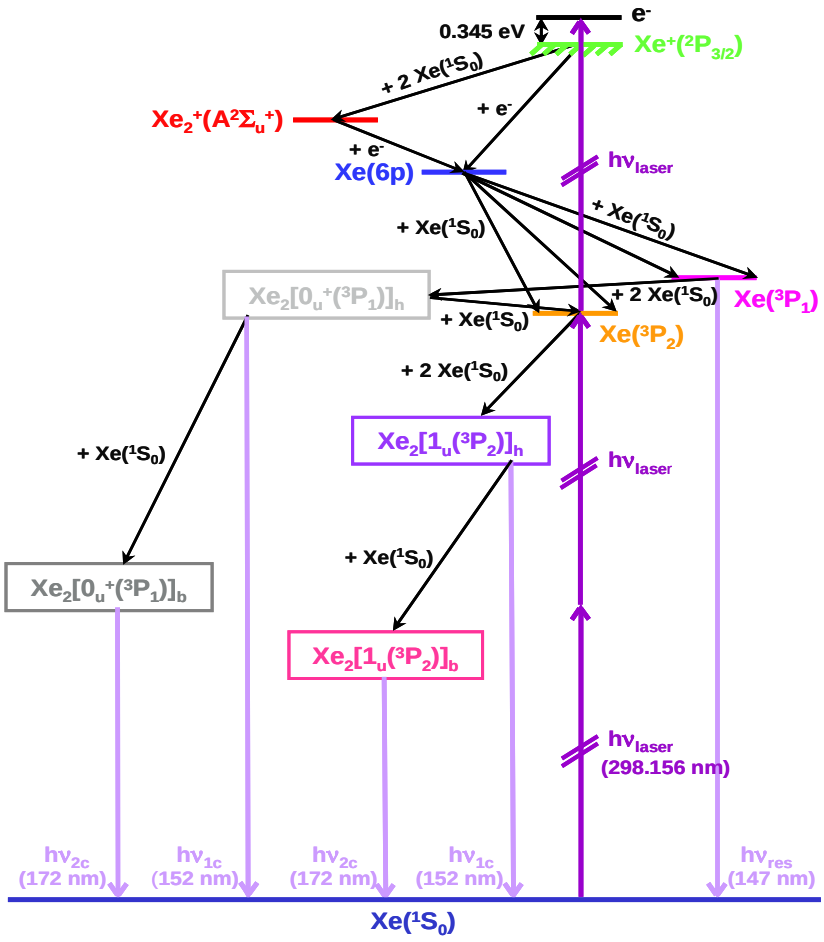
e-
0.345 eV
Xe+(2P3/2)
+ 2 Xe(1S0)
Xe2+(A2Σu+)
+ e-
+ e-
Xe(6p)
hνlaser
+ Xe(1S0)
+ Xe(1S0)
Xe2[0u+(3P1)]h
+ 2 Xe(1S0)
Xe(3P1)
+ Xe(1S0)
Xe(3P2)
+ 2 Xe(1S0)
Xe2[1u(3P2)]h
hνlaser
+ Xe(1S0)
Xe2[0u+(3P1)]b
+ Xe(1S0)
Xe2[1u(3P2)]b
hνlaser
(298.156 nm)
hν2c
(172 nm)
hν1c
(152 nm)
hν2c
(172 nm)
hν1c
(152 nm)
hνres
(147 nm)
Xe(1S0)

Figure 7.

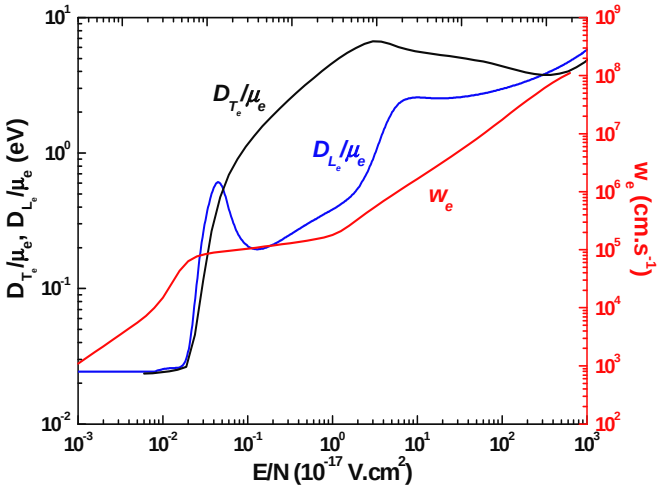

Figure 8.

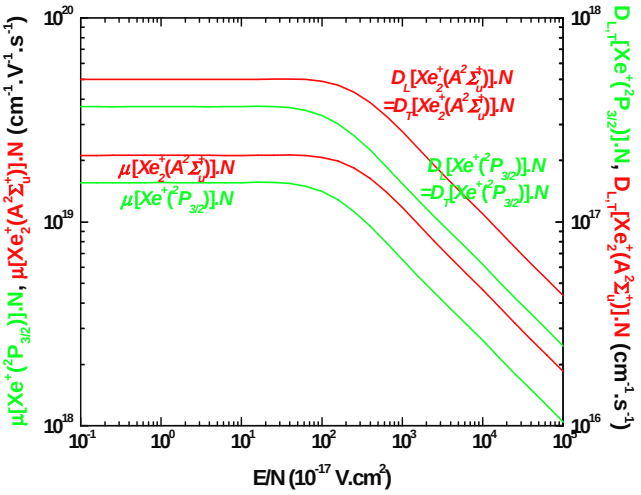
10^{20}
10^{19}
10^{18}
10^{18}
10^{17}
10^{16}
10^{-1}
10^{0}
10^{1}
10^{2}
10^{3}
10^{4}
10^{5}
$D_L[Xe_2^+(A^2\Sigma_u^+)].N$
$=D_T[Xe_2^+(A^2\Sigma_u^+)].N$
$D_L[Xe^+(^2P_{3/2})].N$
$=D_T[Xe^+(^2P_{3/2})].N$
$\mu[Xe_2^+(A^2\Sigma_u^+)].N$
$\mu[Xe^+(^2P_{3/2})].N$
$\mu[Xe^+(^2P_{3/2})].N$, $\mu[Xe_2^+(A^2\Sigma_u^+)].N$ ($cm^{-1}.V^{-1}.s^{-1}$)
$D_{L,T}[Xe^+(^2P_{3/2})].N$, $D_{L,T}[Xe_2^+(A^2\Sigma_u^+)].N$ ($cm^{-1}.s^{-1}$)
E/N (10^{-17} V.cm^2)

Figure 9.

	t = 0 μs	t = 20 μs	t = 50 μs
e^-	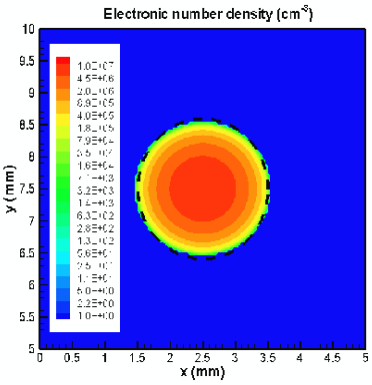	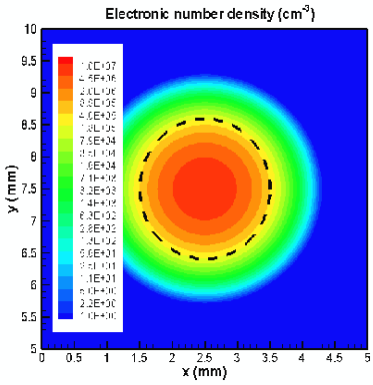	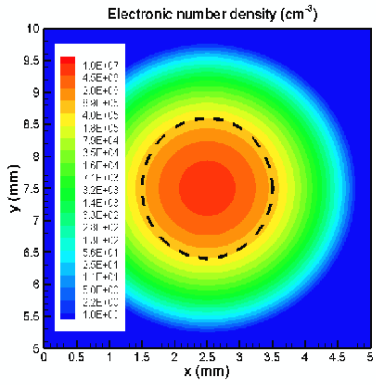
$Xe^+(^2P_{3/2})$	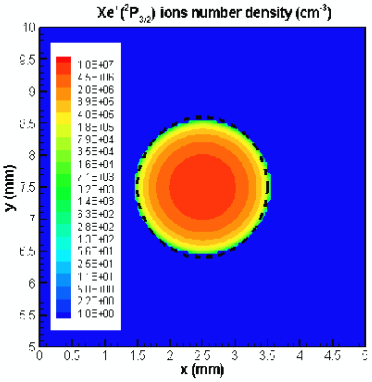	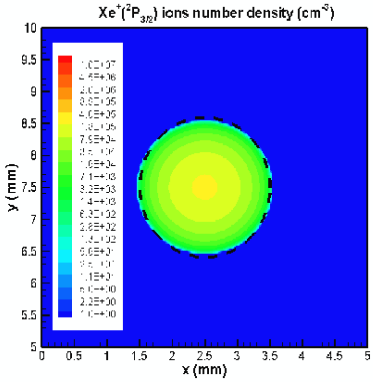	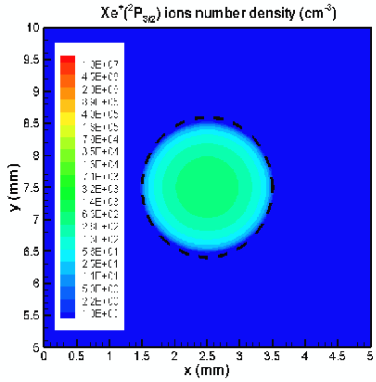
Xe(6p)	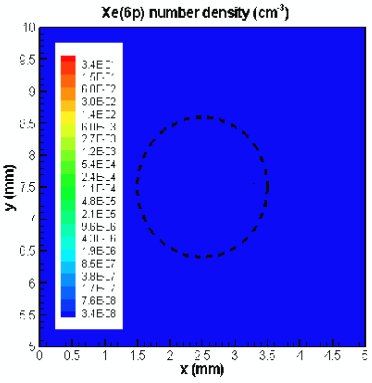	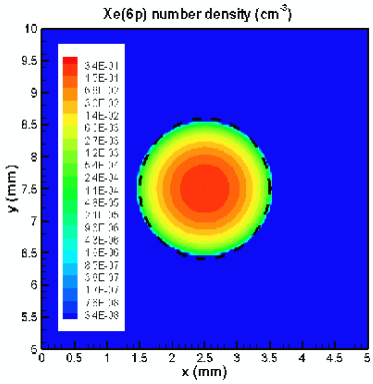	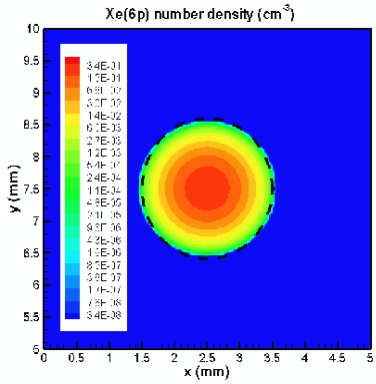

Figure 10.

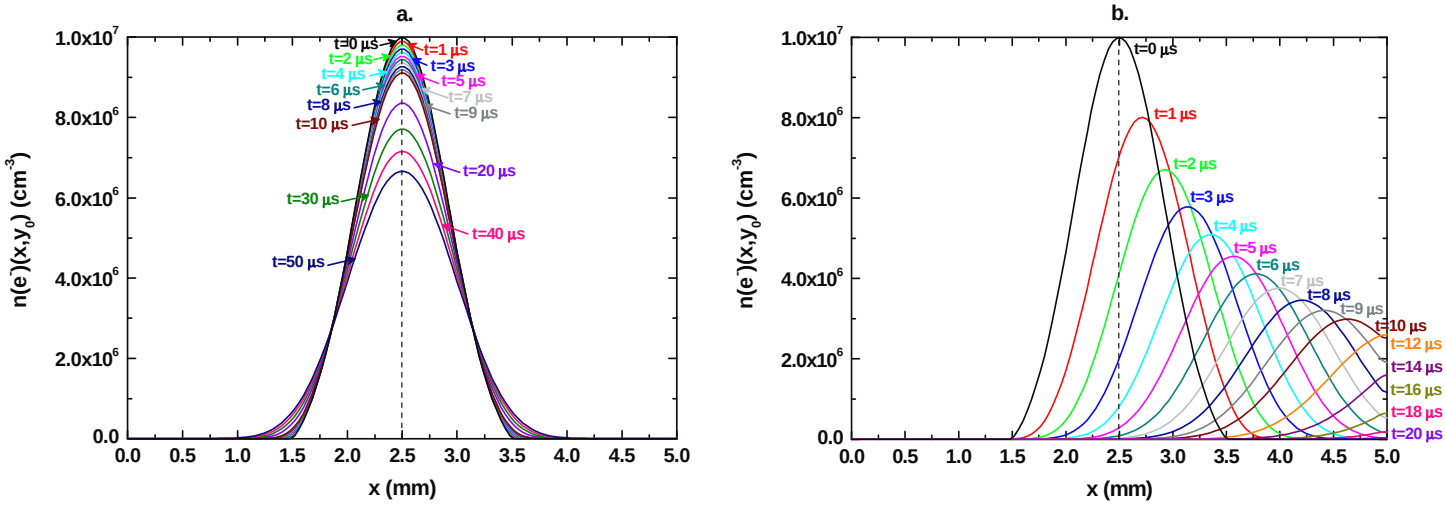

Figure 11.

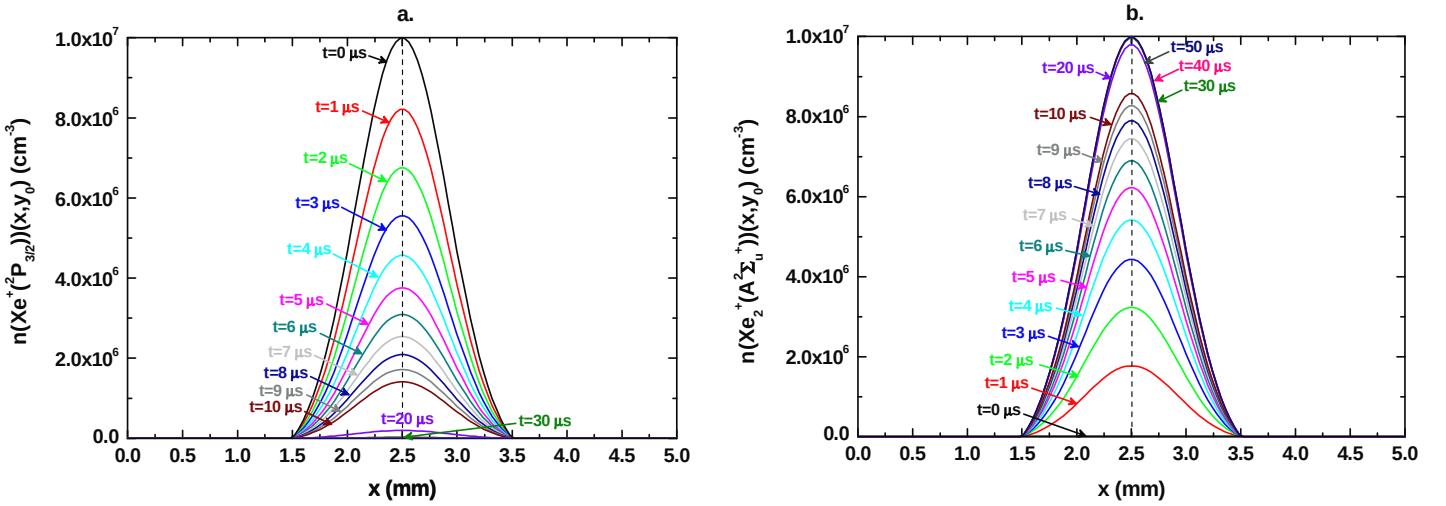

Figure 12.

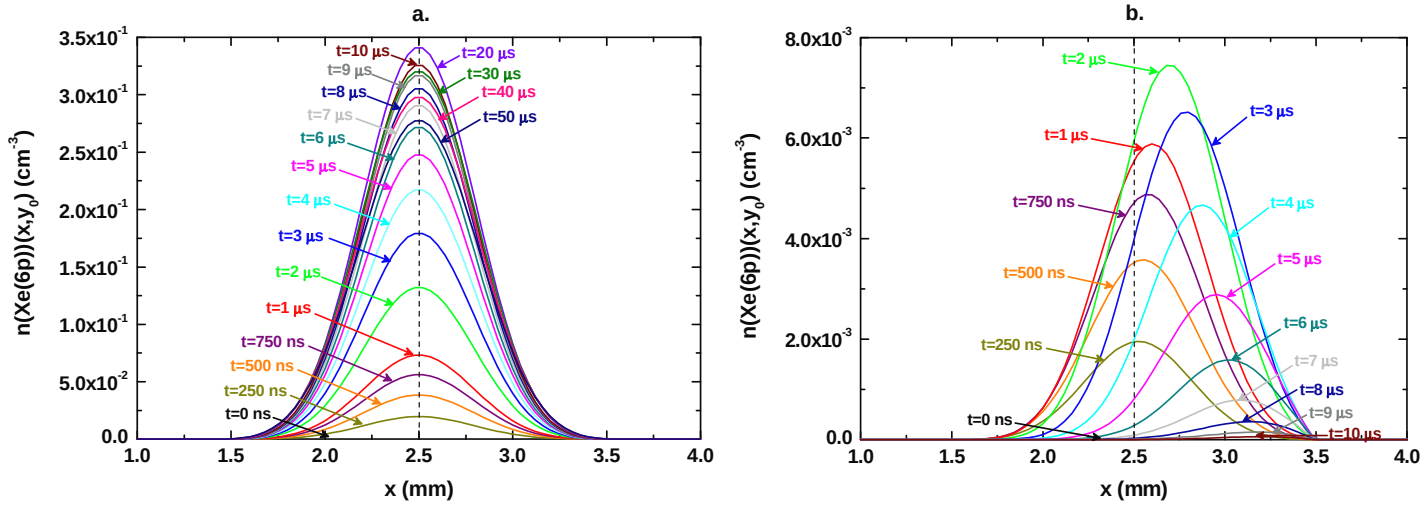

Figure 13.

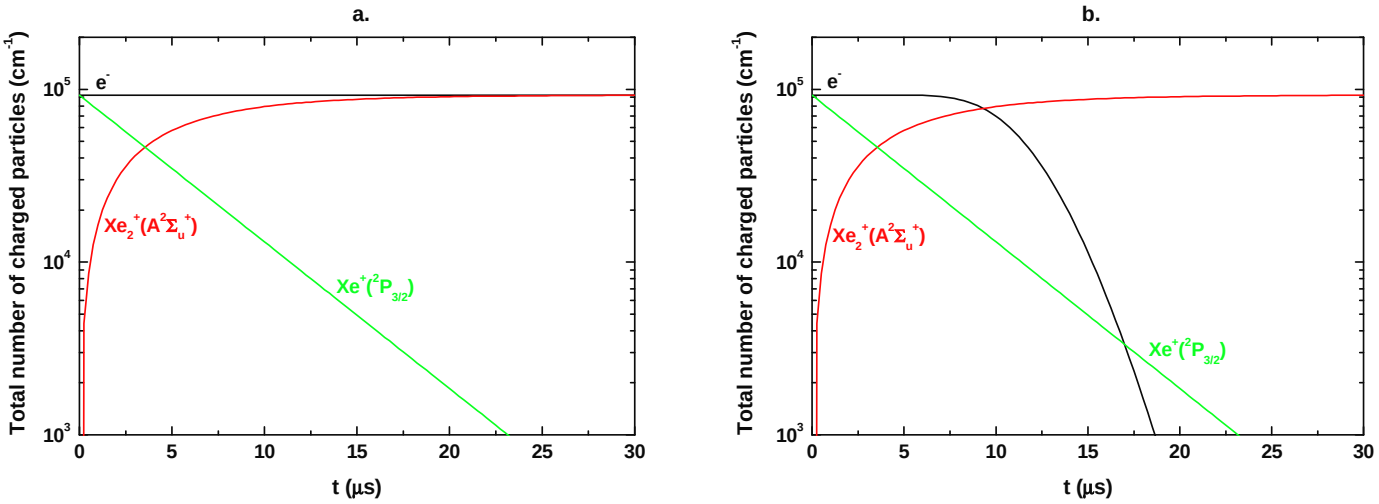

Figure 14.

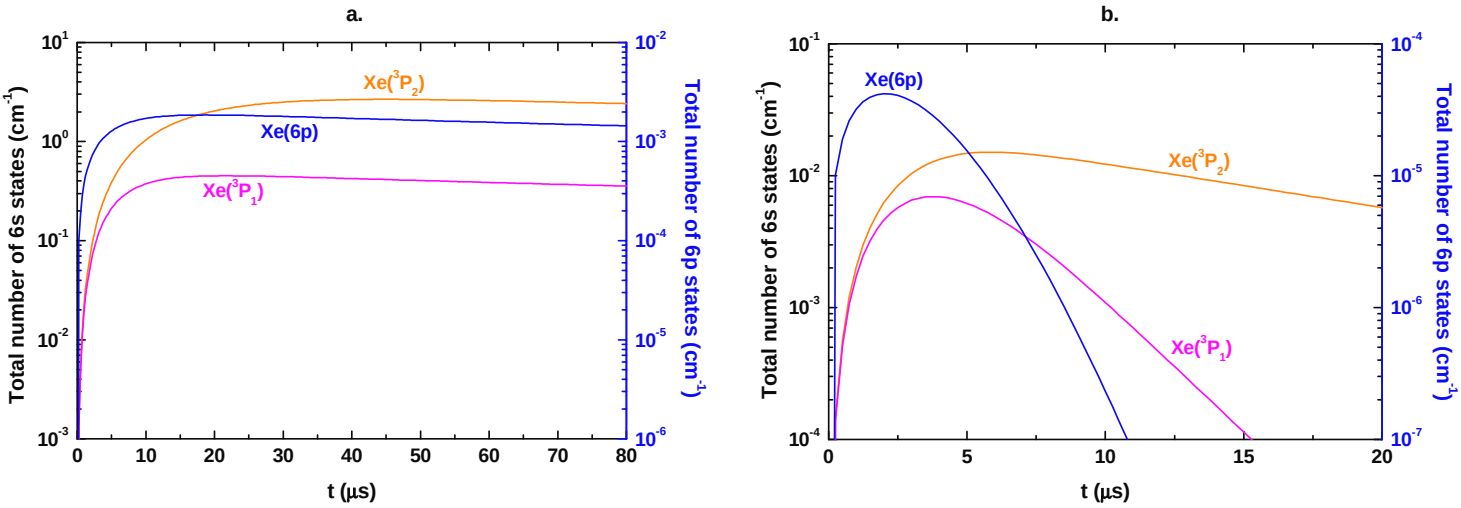

Figure 15.

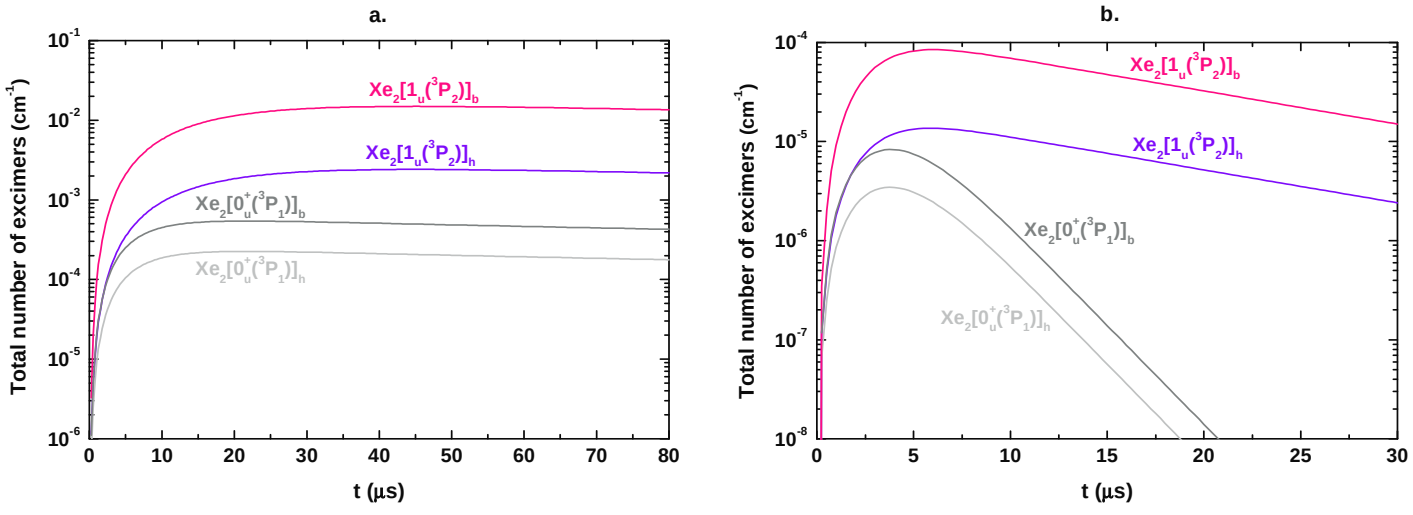

Figure 16.

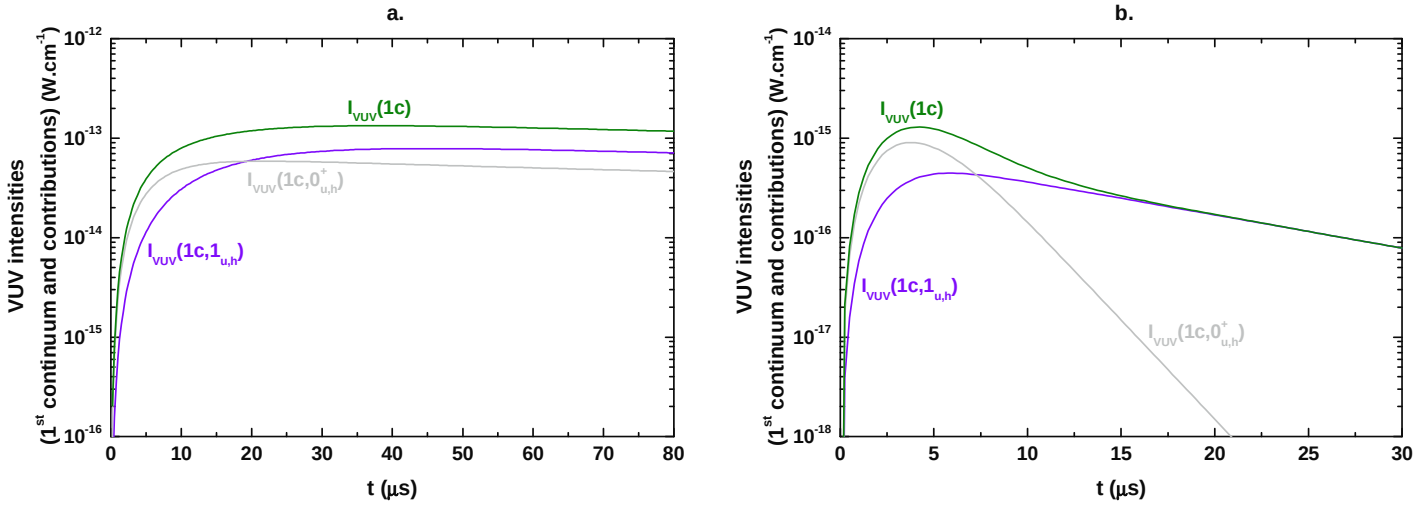

Figure 17.

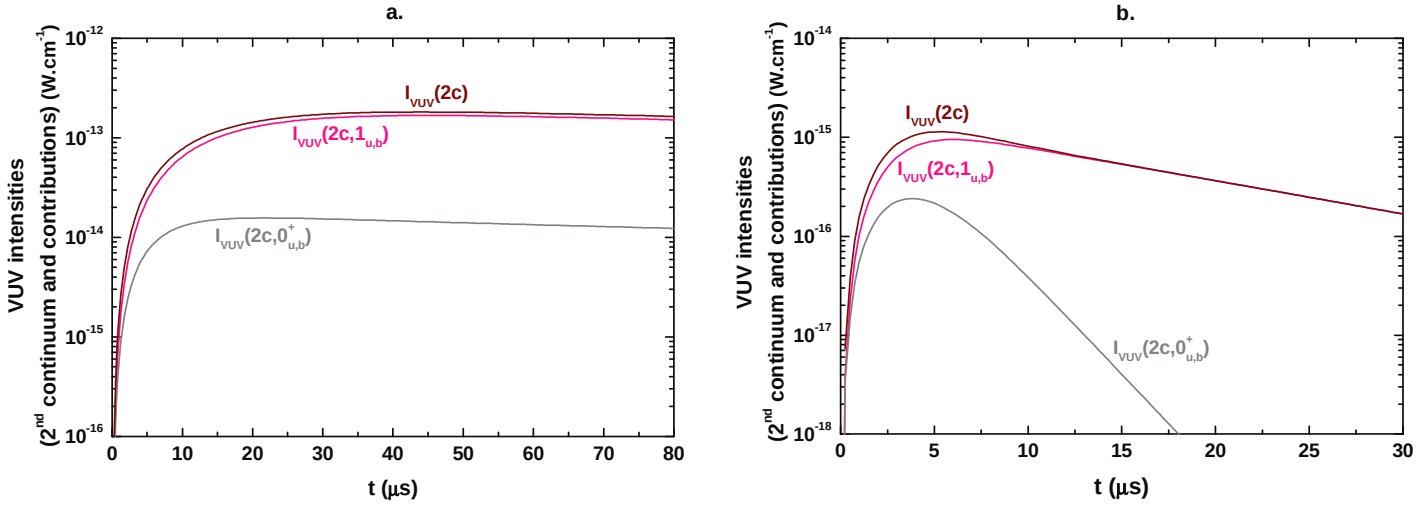

Figure 18.

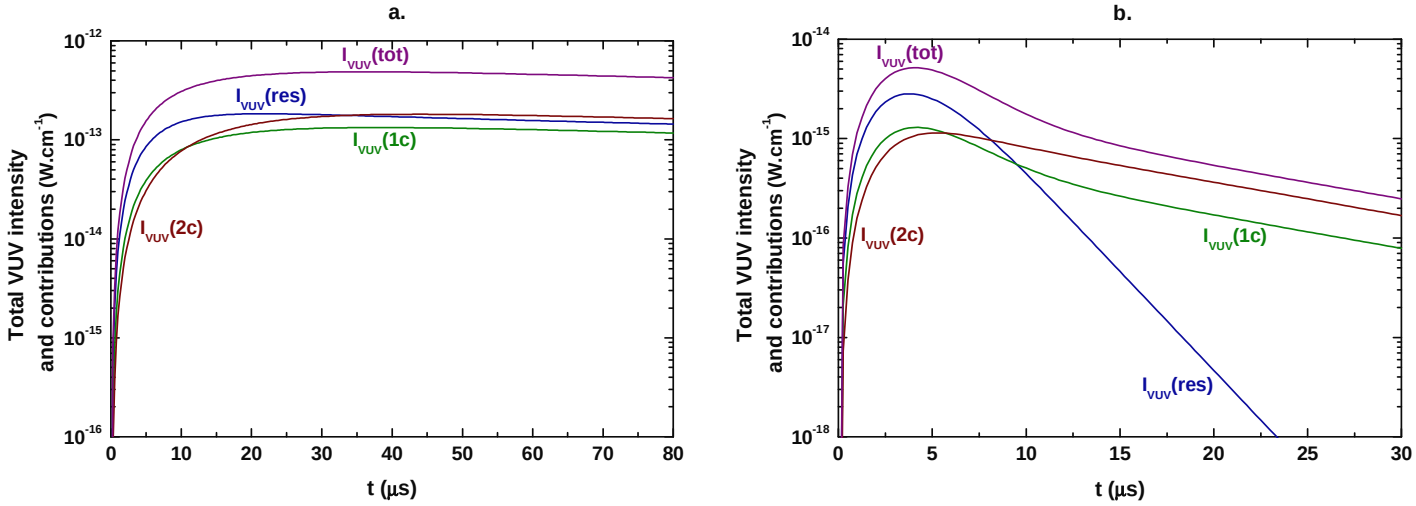

Figure 19.

	t = 0 μs	t = 10 μs	t = 20 μs
e^-	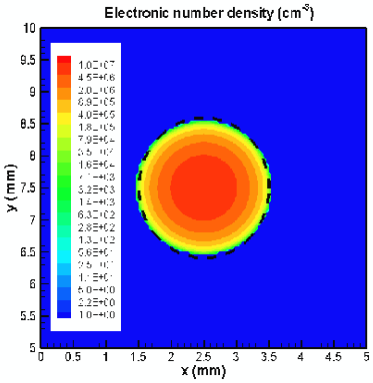	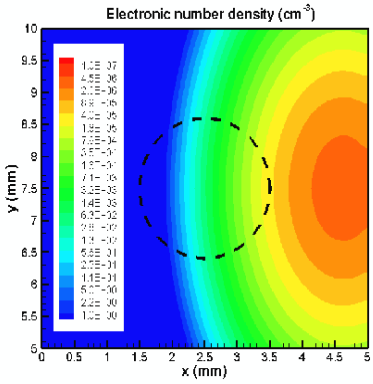	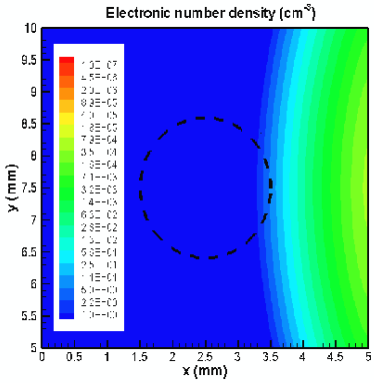
$Xe^+(^2P_{3/2})$	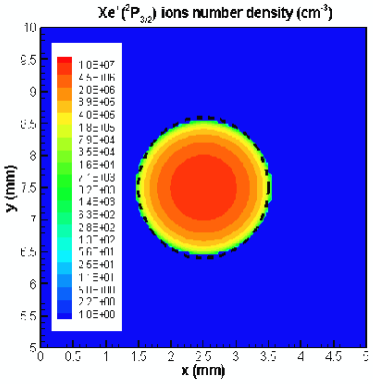	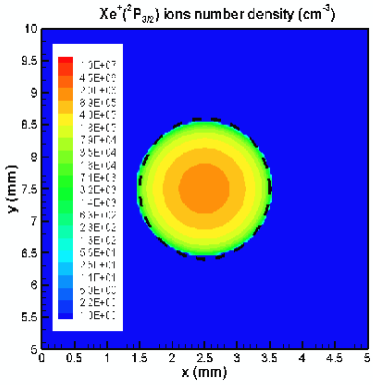	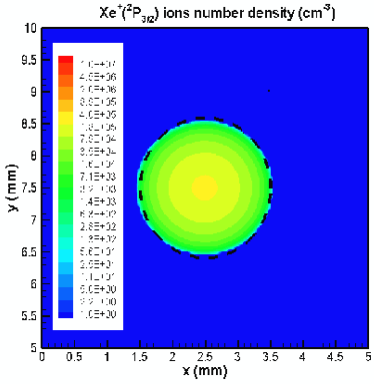
Xe(6p)	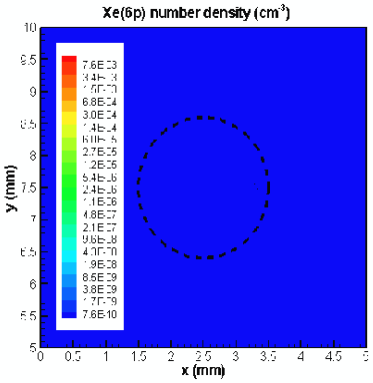	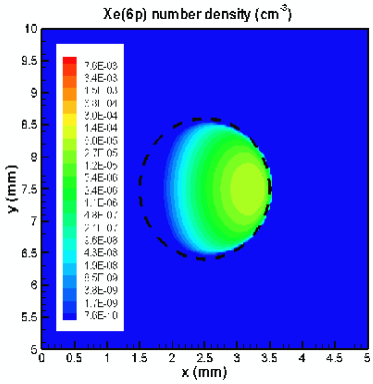	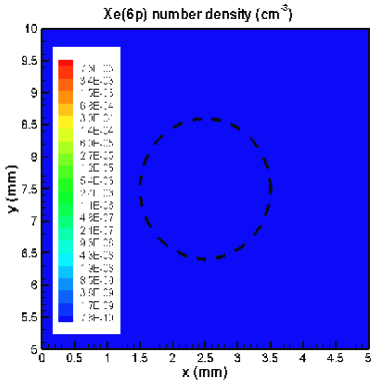

Figure 20.

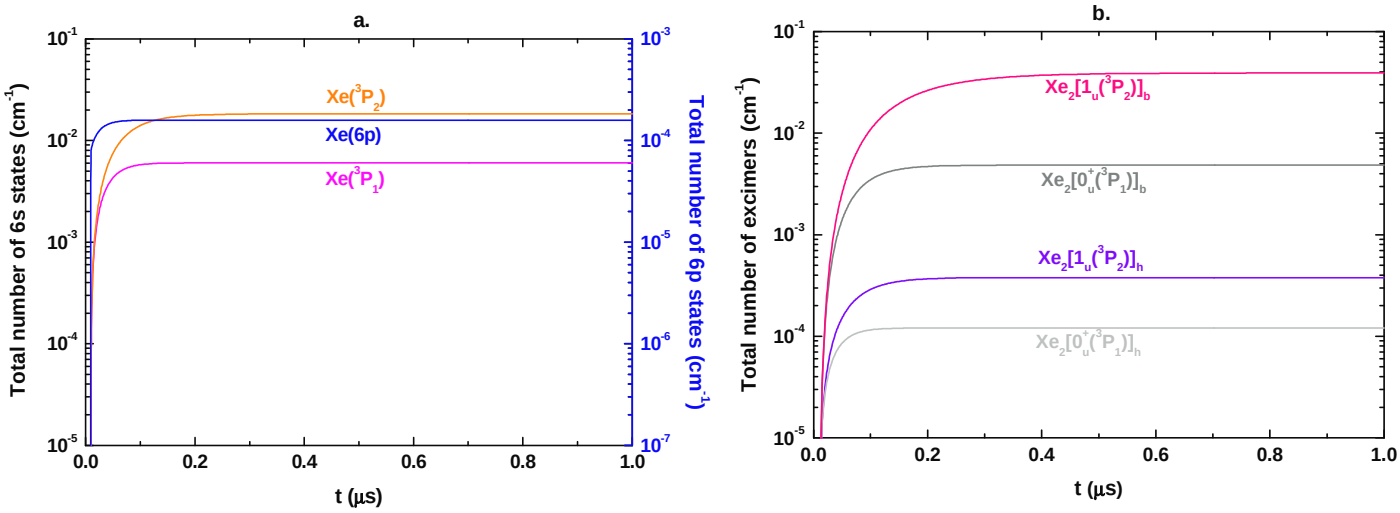
a.
Total number of 6s states (cm-1)
Total number of 6p states (cm-1)
t (μs)
Xe(3P2)
Xe(6p)
Xe(3P1)
b.
Total number of excimers (cm-1)
t (μs)
Xe2[1u(3P2)]b
Xe2[0u+(3P1)]b
Xe2[1u(3P2)]h
Xe2[0u+(3P1)]h

Figure 21.

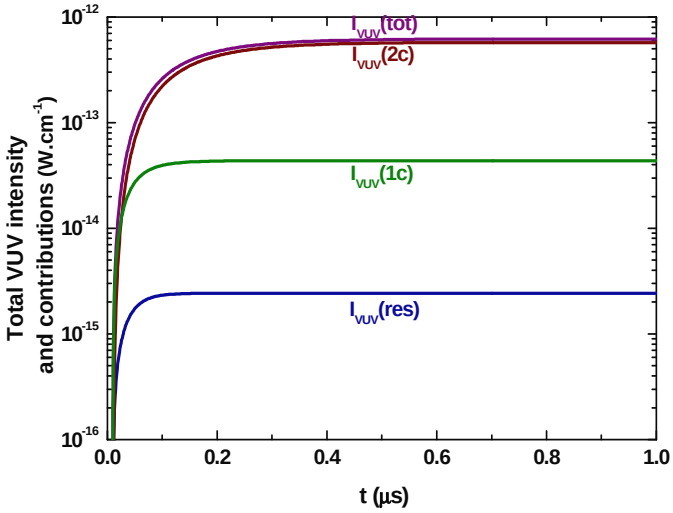
Total VUV intensity
and contributions (W.cm-1)
t (µs)
I_VUV(tot)
I_VUV(2c)
I_VUV(1c)
I_VUV(res)
10-12
10-13
10-14
10-15
10-16
0.0
0.2
0.4
0.6
0.8
1.0